J. Fluid Mech. (1999), vol. 390, pp. 151–185. Printed in the United Kingdom

Study of flow in a planar asymmetric diffuser using large-eddy simulation

By H.-J. KALTENBACH, M. FATICA, R. MITTAL, T. S. LUND AND P. MOIN

Center for Turbulence Research, Stanford University, CA 94305, USA

(Received 11 February 1998 and in revised form 16 January 1999)

Large-eddy simulation (LES) has been used to study the flow in a planar asymmetric diffuser. The wide range of spatial and temporal scales, the presence of an adverse pressure gradient, and the formation of an unsteady separation bubble in the rear part of the diffuser make this flow a challenging test case for assessing the predictive capability of LES. Simulation results for mean flow, pressure recovery and skin friction are in excellent agreement with data from two recent experiments. The inflow consists of a fully developed turbulent channel flow at a Reynolds number based on shear velocity, $Re_\tau = 500$. It is found that accurate representation of the inflow velocity field is critical for accurate prediction of the flow in the diffuser. Although the simulation in the diffuser is well resolved, the subgrid-scale model plays a significant role for both mean momentum and turbulent kinetic energy balances. Subgrid-scale stresses contribute a maximum of 8% to the local value of the total shear stress with the maximum values found in the inlet duct and along the flat wall where the flow remains attached. The subgrid-scale model adapts to the enhanced turbulence levels in the rear part of the diffuser by providing more than 80% of the dissipation rate for turbulent kinetic energy. The unsteady separation excites large scales of motion which extend over the major part of the duct cross-section and penetrate deeply into the core of the flow. Instantaneous flow reversal is observed along both walls immediately behind the diffuser throat which is far upstream of the location of main separation. While the mean flow profile changes gradually as the flow enters the expansion, turbulent stresses undergo rapid changes over a short streamwise distance along the deflected wall. An explanation is offered which considers the strain field as well as the influence of geometry changes. The effect of grid resolution and spanwise domain size on the flow field prediction has been documented and this allows an assessment of the computational requirements for carrying out such simulations.

1. Introduction

With increasing computing power more complex flow configurations are being investigated by means of three-dimensional, unsteady numerical simulation. The large-eddy simulation (LES) technique, in which resolved and subgrid-scale motions are defined by a spatial filter applied to the Navier–Stokes equations, has emerged as a promising tool which complements Reynolds-averaged Navier–Stokes (RANS) computations.

The development of the dynamic model for subgrid-scale (SGS) stresses by Germano *et al.* (1991) was a major advance towards a general model which is applicable

to an arbitrary flow without requiring adjustment of model parameters. Recent wall-resolving simulations of channel flow at Reynolds numbers up to $Re_\tau = 4000$ have demonstrated the self-consistency and potential of this model (Kravchenko, Moin & Moser 1996). The dynamic model has been used for simulation of a variety of complex flows such as boundary layer development along a concave wall (Lund & Moin 1996), flow separation behind a step and in a co-axial pipe expansion (Akselvoll & Moin 1995, 1996) and bluff body wakes (Mittal & Moin 1997). Recent developments in SGS modelling are described in Ghosal *et al.* (1995) and Lesieur & Metais (1996).

The outcome of an actual LES will depend not only on the quality of the SGS model but may be influenced by the numerical method used to solve the equations for the resolved scales (Ghosal 1996 ; Mittal & Moin 1997). Because of the intricate problem of separating the effects of SGS model and numerical approximation it is necessary to assess the quality of a simulation technique by evaluating its capability to predict flows for which detailed measurements are available.

Pressure-driven separation from a smooth wall defines an important class of flows for which few results using the LES technique have been reported. Mildly separated flows have always been challenging for experimentalists as well as modellers. Spanwise homogeneity of turbulence in an experimental setup of a nominally two-dimensional separated flow is only achieved when great care is taken to ensure the incoming flow is uniform in the cross-stream direction (Alving & Fernholz 1996). Often, experimentalists have to adjust sidewalls, vary suction streams in the span or use flow guiding vanes and other devices to enforce two-dimensionality of the mean flow in the presence of separation (Simpson, Chew & Shivaprasad 1981). The presence of sidewalls can prevent the flow from being homogeneous in the case of a region with strong backflow (Ruderich & Fernholz 1986). Dengel & Fernholz (1990) found the mean location of separation as well as the extent of the flow reversal zone to be extremely sensitive to small changes in the upstream pressure distribution.

Research on separated flow physics has been hindered by the fact that the conventional hot-wire measurement technique is direction insensitive and requires a significant mean flow component to produce reliable measurements. With increasing use of the LDA technique more data for separated flows are becoming available which are suitable for validation purposes. Most of the earlier work on separating flows is summarized in Simpson (1989). More recent studies include the work by Alving & Fernholz (1996). In addition, Na & Moin (1998) performed a direct simulation of a separated boundary layer with a closed separation bubble. They found that the flow detachment is a highly unsteady process and the zone where the boundary layer separates from the wall exhibits patches of local backflow rather than a single line which separates the forward from backward flows. The unsteady motion of the bubble could be characterized by a Strouhal number based on the displacement thickness of the incoming flow and this was found to be in the range 0.0025 to 0.01.

Numerical simulation of flow separation from smooth surfaces have been carried out in the context of flow over wavy walls where surface curvature and upstream flow history are known to affect the flow development. While the agreement of DNS of flow over wavy walls with available measurements is good (Mass & Schumann 1996; De Angelis, Lombardi & Banerjee 1997), prediction based on LES in conjunction with a near-wall model appears to be less reliable (Gong, Taylor & Dörnbrack 1996).

A particularly interesting configuration was investigated experimentally by Obi *et al.* (1993*a*) and Obi, Aoki & Masuda (1993*b*) using a single-component laser-Doppler anemometer (LDA): a fully developed turbulent flow from a long inlet duct enters

a plane, asymmetric diffuser with an opening angle of 10°. The flow separates about halfway down the deflected wall and a separation bubble forms which extends into the straight outlet duct where the flow reattaches.

This flow has several desirable features which make it a good test case for validation of a computational technique such as large-eddy simulation:

(*a*) The flow belongs to the class of 'mild', pressure-driven separation from a smooth wall. Many technical devices are designed to operate close to these conditions since optimum performance is often achieved when the flow is at the verge of separation (Ashjaee & Johnston 1980).

(*b*) The flow exhibits rich flow physics, such as the combined effects of adverse pressure gradient and convex curvature near the diffuser inlet and incipient separation and reattachment in the outlet duct.

(*c*) The inflow conditions are unambiguously defined. The inlet duct has a length of more than 100 duct heights, thereby guaranteeing that the flow entering the expansion is fully developed turbulent channel flow. Flow in a duct with parallel walls has been studied extensively using LES and the requirements in terms of grid spacing and SGS model are documented (Cabot 1994; Piomelli 1993; Kravchenko *et al.* 1996). For validating the computation of a spatially evolving flow it is crucial to know the statistics of the upstream flow with a high degree of accuracy. Lund & Moin (1996) found that seemingly small variations in upstream conditions can cause significant downstream differences in a spatially evolving flow.

(*d*) The Reynolds number of the incoming channel flow is 9000 based on the half-width of the inlet duct and bulk velocity. This corresponds to a wall-shear-based Reynolds number close to $Re_\tau = 500$. Although a direct simulation of channel flow is feasible at this Reynolds number, a DNS of the full diffuser is still prohibitively expensive. The Reynolds number is high enough that the flow is insensitive to this parameter. S. Obi (1994, personal communication) did not observe significant changes in flow physics when doubling the Reynolds number.

During the course of the work, a closer examination of the experimental dataset from Obi *et al.* (1993*a*) revealed some inconsistencies. Basic requirements such as mass and momentum balances of the two-dimensional mean flow were not met in the rear part of the expansion (Kaltenbach 1994). As a result, it was felt that an independent confirmation of the experimental data was highly desirable. Therefore, a configuration similar to Obi's rig was built and great care was taken to ensure that the data satisfied basic requirements for validation (Buice & Eaton 1996, 1997).

The main motivation for this study comes from the need to validate the technique of wall-resolving LES with the dynamic model in the case of a spatially evolving flow with mild separation. The first part of this article will be devoted to this issue. In the second part we focus on the flow physics with emphasis on the unsteady processes which are characteristic of flow separation from a smooth wall.

We will also examine our database with respect to turbulence statistics which are of interest in the context of RANS modelling. Obi *et al.* (1993*b*) demonstrated that the standard $k-\epsilon$ model fails to predict the extent of separation inside the diffuser. They obtained better agreement with measurements using a second-moment closure. Recently Durbin (1994) successfully computed the present diffuser flow using his $V2F$ model in conjunction with the elliptic relaxation procedure.

The paper is organized as follows: after describing the simulation technique in §2 we discuss in detail the suitability of the two experimental data sets for validation purposes (§3.1). In §3.2 we compare simulation and measurements. Section 4 deals with computational aspects such as sensitivity of the results to domain width

and resolution. Finally, § 5 is devoted to detailed examination of flow physics, and conclusions are presented in § 6.

2. Numerical method

The code is based on a hybrid second-order finite difference/spectral method which solves the three-dimensional incompressible Navier–Stokes equations in primitive variables (velocity and pressure) in generalized coordinates on a spanwise periodic domain. Central finite differences of second-order accuracy were used in the streamwise and wall-normal directions whereas Fourier collocation was used in the spanwise direction. The Fourier discretization method provides better spanwise resolving power and it was found to be a cost effective alternative to the second-order method with increased number of spanwise grid points. The scheme was constructed to ensure conservation of the kinetic energy which allows a stable computation without the need for numerical dissipation which would have had a significant impact on the smaller resolved scales (Mittal & Moin 1997). A staggered mesh is used in the plane of the generalized coordinates with volume fluxes, i.e. contravariant velocity vector components weighted with the Jacobian as dependent variables (Orlandi 1989; Rosenfeld, Kwak & Vinokur 1991; Choi, Moin & Kim 1992). The spanwise velocity component is collocated at the pressure nodes. Phase-shifting dealiasing (Rogallo 1981) is performed in order to stabilize the computations and enhance accuracy.

Although previous simulations used a fully implicit method (Kaltenbach 1994), the time step in this flow is limited mainly by the turbulence time scale in the inlet duct and not by numerical stability considerations. Thus, much of the potential benefit of using an implicit scheme is not fully realized in this case. The solution is advanced in time by a semi-implicit scheme where the viscous terms in the wall-normal direction are integrated by means of the Crank–Nicholson method and all other terms are integrated with a low-storage third-order Runge–Kutta scheme (Spalart, Moser & Rogers 1991).

The incompressibility constraint is enforced with a time-split technique which is second-order accurate in time. By taking Fourier transform in the spanwise direction, the pressure Poisson equation is reduced to a series of two-dimensional Helmholtz equations, one for each spanwise wavenumber. Each of these equations is then solved with a multigrid technique. The time step used for these computations is about $\Delta t = 0.04\delta/U_b$. On a Cray C90 20 μs are needed per cell to advance the computation one time step. A quarter of the total effort is spent on the Poisson solver.

The subgrid-scale model used to account for the effect of the unresolved turbulent motions is a version of the dynamic model suitable for generalized coordinates. A least-square contraction (Lilly 1992) is used to compute the model coefficient which is obtained as a spanwise averaged quantity. The test filter is applied in the streamwise and spanwise directions using the trapezoidal rule to approximate the filter, and the test-to-grid filter ratio is $\hat{\Delta}/\Delta = \sqrt{6}$.

The present numerical method and the associated computer program have been tested extensively in several laminar and turbulent flows (Orlandi 1989; Choi *et al.* 1992; Wang, Lele & Moin 1996; Mittal & Moin 1997).

2.1. *Boundary conditions*

No-slip boundary conditions are applied along the solid walls and the spanwise direction is treated as periodic. At the inlet plane we specify unsteady Dirichlet boundary conditions for the velocity components which were generated by an independent LES

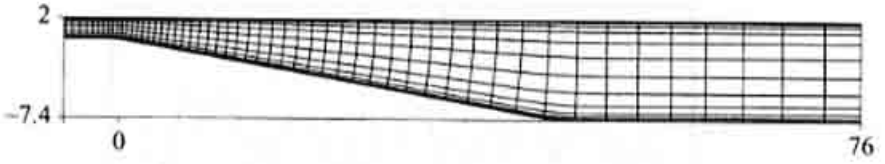

FIGURE 1. Computational domain for the plane diffuser. Only a subset of the actual grid lines is plotted.

				$\Delta x/\delta$ at $x/\delta =$						
Case	N_x	N_y	N_z	−5	0	10	30	50	L_z	$\Delta z/\delta$
COARSE	160	64	64	0.24	0.14	0.31	0.65	1.0	4δ	0.063
MED-N	272	64	64	0.1	0.05	0.22	0.56	0.82	4δ	0.063
MED-W	272	64	96	0.1	0.05	0.22	0.56	0.82	8δ	0.083
FINE	352	64	128	0.063	0.052	0.17	0.41	0.6	8δ	0.063

TABLE 1. Grid spacings $\Delta x, \Delta z$ and domain width L_z used in simulations. N_x, N_y, N_z denote the number of cells in streamwise, wall-normal and spanwise direction, respectively.

of a fully developed channel flow. At the diffuser exit plane a convective boundary condition

$$\frac{\partial u_i}{\partial t} + U_c \frac{\partial u_i}{\partial x} = 0 \tag{2.1}$$

is used. The convection speed U_c is set equal to the mean streamwise velocity integrated across the exit plane.

2.2. *Flow configuration*

The diffuser geometry as shown in figure 1 and Reynolds number $Re_b = U_b\delta/\nu = 9000$ match the experimental configuration of Obi *et al.* (1993*a*) and Buice & Eaton (1997). Here, the Reynolds number is based on the bulk velocity U_b found in the inlet duct of height 2δ. The corresponding Reynolds number based on wall shear is $Re_\tau = 500$. The upstream corner, formed by the inlet channel wall and the deflected wall, marks the origin of the underlying coordinate system. The inlet plane is located at $x/\delta = -5$ where the upstream influence of the expansion is negligible. The parallel flow from the inlet duct enters the asymmetric diffuser characterized by an expansion ratio $a = h_{out}/h_{in} = 4.7$ and by an opening angle of 10°. Both the upstream and downstream corners are rounded with a radius of 8.6δ. The expanding section extends over 42δ and is followed by a tail duct of height 9.4δ and a length of approximately 30δ. The exit plane is located near $x/\delta = 75$. At this location the flow has reattached but is far from being in equilibrium. The focus of the present study is separation and reattachment and not the recovery into a canonical channel flow which occurs over a length of tens of heights of the tail duct (Buice & Eaton 1997).

Simulations were performed on three different meshes and for domain widths of 4δ and 8δ in the spanwise direction. The mesh is stretched in the streamwise and wall-normal directions and designed such that the streamwise spacing gradually decreases towards the diffuser throat at $x/\delta = 0$. Inside the expansion the spacing increases with downstream distance from the diffuser throat. We will compare results from a set of four simulations for which computational parameters such as grid spacing and domain width were varied in a systematic manner, see table 1. Except for the coarsest

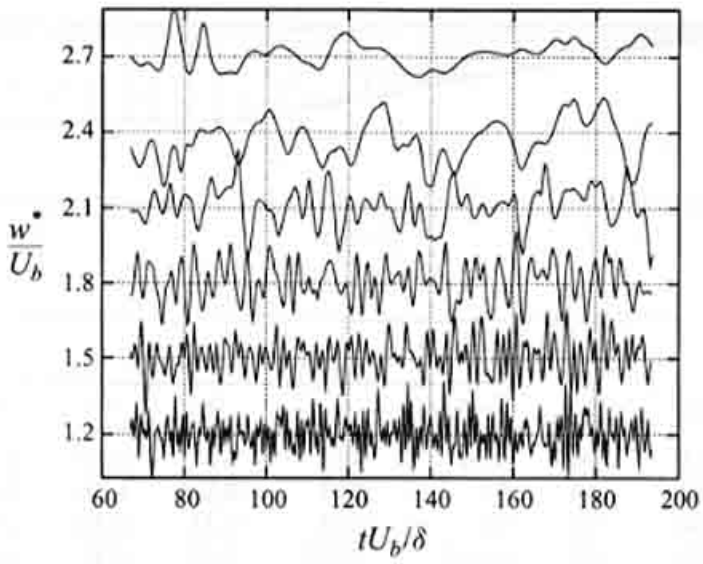

FIGURE 2. Temporal evolution of the spanwise velocity component w^*/U_b recorded close to the diffuser centreline at locations: $x/\delta = 5, 8, 12, 17, 24, 33, 43$ (from bottom to top). The offset between consecutive zero lines is 0.3.

mesh, the spacing in the inlet duct matches the grid of the corresponding channel flow simulation which created the inflow data.

Computationally, this flow is very challenging because of the large range of time scales encountered. The inertial time scale $\tau = 0.5h(x)/U_b(x)$, based on local diffuser height $h(x)$ and bulk velocity $U_b(x)$, is proportional to the square of the expansion ratio, i.e. $\tau_{out} = a^2\tau_{in}$ (with $a^2 = 4.7^2 = 22.1$). At the same time, the computational time step is limited by the need to resolve the turbulence in the inlet section. The net effect of the time-scale disparity is that the simulations require lengthy integration times. The change in time scales is evident in a plot of recorded time series (figure 2). Before sampling statistics, the simulation is run long enough to ensure that initial transients have been flushed out. Statistics are then sampled over a period of $1280\,\tau_{in}$ for case FINE. On average, a fluid particle requires between $\int_0^{L_x} U_{max}^{-1}(x)\,dx \approx 160\,\tau_{in}$ and $\int_0^{L_x} U_b^{-1}(x)\,dx \approx 290\,\tau_{in}$ to travel through the domain. The time-averaging window is long enough to ensure converged statistics in the rear part of the diffuser where we observe a low-frequency unsteadiness with a time scale close to $100\,\tau_{in}$.

Statistics are formed by averaging in the spanwise direction as well as time, a combined operation denoted by an overbar. An instantaneous value u^* is decomposed into a mean value and a fluctuation which are denoted by upper and lower case letters, respectively, i.e. $u^* = U + u$ with $\overline{u^*} = U$. The subscript *rms* denotes the root-mean-square value of a fluctuating quantity, i.e. $u_{rms} = \sqrt{\overline{u^2}}$. If not stated explicitly, all statistical quantities obtained from the simulation refer to the *resolved scale* (grid-scale, filtered) quantities (i.e. u^* above is a resolved-scale velocity).

3. Validation of simulation results

The present work aims at exploring the capability of LES for accurate quantitative prediction. For this purpose we compare simulation results with measurements from Obi *et al.* (1993*a*, *b*) and Buice & Eaton (1997). For simplicity we refer from now on to the Obi and the Buice experiments, respectively.

3.1. *Evaluation of experimental data sets*

A meaningful comparison between simulation and experiment hinges on the assumption that the same flow is being studied. Ideally, this requires a match in geometry, inflow and outflow conditions, and Reynolds number. At the present state of high-resolution numerical simulations, it is not yet possible to compute the entire spanwise extent of the diffuser, including the sidewalls. Thus we choose to idealize the flow as being homogeneous in the spanwise direction, a situation that would be realized only in the limit of infinite aspect ratio. This assumption allows us to use a uniform mesh and periodic boundary conditions applied to a limited domain in the spanwise direction. As a consequence, highly accurate Fourier-expansion-based methods can be used. Furthermore, statistical averaging in the homogeneous direction reduces the required sampling time considerably, resulting in significant savings in CPU time. The assumption of homogeneity is valid in as much as the flow can be considered statistically two-dimensional. The periodic boundary condition will pose a negligible constraint on the flow dynamics provided that the computational box is sufficiently large when compared with the turbulence integral scale. Fortunately, considerable care was taken in both of the experimental programs used here for comparison to ensure that the flow was nearly two-dimensional. The computational box size was chosen to be as large as possible in order to minimize the effect of the periodic boundary condition. Nonetheless, deviations from the stated assumptions do exist and we shall spend considerable effort in the following sections isolating the regions where a fair comparison between simulation and experiment can be made.

To set up an experimental study of a separated flow which exhibits spanwise homogeneity remains a challenge. Once the flow separates, the inherent three-dimensionality resulting from the sidewalls of an experimental facility often increases significantly (Simpson *et al.* 1981; Ruderich & Fernholz 1986). By choosing configurations with wide aspect ratios it is hoped that effects from unavoidable secondary flows will be small and will not affect the core region which should represent a nominally two-dimensional flow.

3.1.1. *Assessment of suitability of Obi's data for validation*

Obi *et al.* (1993*a*, *b*) investigated flow in an asymmetric diffuser at $Re_b = 8800$ using LDA in a wind tunnel. They measured pressure along the flat wall, mean velocity profiles, and Reynolds stresses. The inlet channel height was 20 mm and the aspect ratios of the diffuser inlet and outlet were 1:35 and 1:7.45, respectively. The inlet channel was slightly wider than the diffuser in order to remove the thick sidewall boundary layers before entering the expansion. Buice & Eaton (1997) employed the same technique. In order for the fluid to enter the side slots, the pressure in the slots has to be slightly lower than the ambient pressure. Buice achieved this by slightly obstructing the diffuser exit, thereby raising the average pressure level in the diffuser. A similar strategy was not reported for the Obi experiment.

Measurement errors for U and Reynolds stresses in the Obi experiment are estimated to be 0.7% and 2.6% respectively (Maeda *et al.* 1995). Mean flow profiles are two-dimensional to within 5% of U over 90% of the inlet duct and 60% of the outlet. The mean flow profile measured 22δ upstream of the diffuser throat in the inlet channel is slightly asymmetric. However, the ratio of centreline to bulk velocity at this location is 1.14 which matches closely the prediction of Dean (1978) for fully developed channel flow.

The flow-rate per unit width $m = \int U(y)\,dy$ computed from profiles measured along the centre-plane is plotted in figure 3. Up to the end of the expansion near

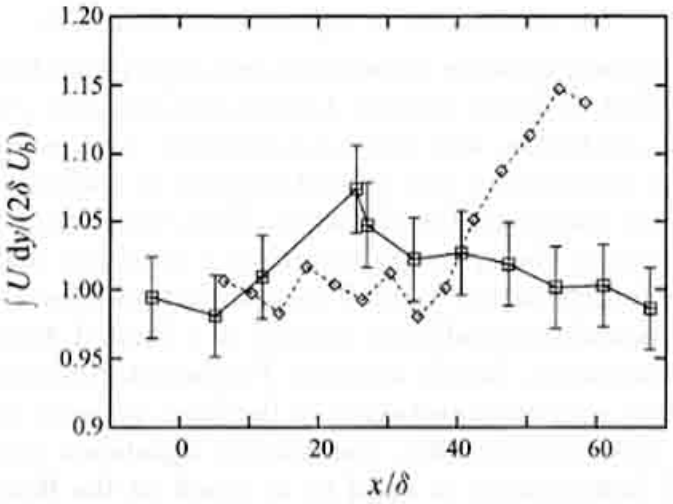

FIGURE 3. Flow rate $\int U\,dy/(2\delta U_b)$ from experiments by Obi (◇) and Buice (□). U_b is the bulk velocity of the inlet channel. Error bars mark ±3% deviation.

$x/\delta = 40$ the flow rate is constant to within a 2% error band. As the flow leaves the expansion and enters the tail duct the flow rate increases rapidly. This might indicate that significant secondary flow develops in the tail duct. Available profiles for mean flow and turbulence statistics were scaled in a way such that global mass conservation is guaranteed at every station (Maeda *et al.* 1995). We will use Obi's scaled data for comparison with simulation results, keeping in mind that profiles measured downstream of $x/\delta = 40$ have only qualitative value for validation.

A special remark is required with respect to proper normalization of pressure measurements which are published in Obi *et al.* (1993*b*). There, c_p is given with respect to a reference velocity U_{ref}. Since we choose to present our data with respect to the bulk velocity of the incoming channel flow we need to know the ratio U_{ref}/U_{bulk}. Obi *et al.* (1993*b*) state that the reference velocity was the centreline velocity of the inlet duct. However, the mean flow profile measured in the inlet duct at $x/\delta = -22$ reaches a peak of $0.975U_{ref}$ (see Maeda *et al.* 1995). Thus, $U_{ref} = 1.025U_{cent}$ and with $U_{cent}/U_{bulk} = 1.14$ the conversion of c_p given with respect to U_{ref} into c_p with respect to U_{bulk} involves multiplication with the square of $U_{ref}/U_{bulk} = 1.168$. Obi (1997, personal communication) has corroborated recently that U_{ref} is indeed 2.5% higher than the centreline velocity from the inlet duct. He attributes this to the fact that a hot wire was used to measure U in the inlet duct whereas LDA was used elsewhere.

3.1.2. *Experiment by Buice & Eaton*

The overall dimensions of the experimental facility of Buice & Eaton (1997) are similar to Obi's setup. The novel feature of this experiment is that the pressure level in the facility was raised through exit blockage, thereby allowing careful control of sidewall boundary layer leakage through slots immediately ahead of the throat. With this method a realistic pressure gradient in the inlet duct is achieved (figure 8), thereby defining the upstream conditions in an unambiguous manner. Velocity was measured with the hot-wire technique, using single and cross-wires in regions with significant forward flow and pulsed wires elsewhere. The maximum error in the mean velocity was estimated to be 3%. Flow rates obtained from integration of velocity profiles measured† with a single wire upstream of separation and a combination of single

† For technical reasons, data at $x/\delta = 25.5$ have a higher uncertainty than at other stations and have therefore been omitted from the compilation of Buice & Eaton (1997).

and pulsed wires elsewhere are plotted in figure 3. An increase in flow rate of the order of 5% occurs locally in the vicinity of $x/\delta = 25$, i.e. immediately behind the zone of maximum pressure rise. Wool tufts mounted on the sidewalls did not indicate the presence of secondary flow or sidewall separation. Yet, the mass-flow deviation in this region is slightly greater than the confidence level for the measurements. No check of spanwise homogeneity at this location is available. Downstream of $x/\delta = 34$ the mass is globally conserved to within 3% and the flow is uniform in the span to within 3%.

3.1.3. *Force balance*

The integral momentum balance for a fixed control volume reads for the time- and spanwise-averaged force component F_x per unit depth

$$\sum F_x = (F_{p,out} - F_{p,in}) + F_{p,ramp} + F_{fric} + (F_{visc,in} - F_{visc,out}) = M_{in} - M_{out}.$$

The corresponding control volume consists of vertical cuts at $x_{in} = -4\delta$ and at a downstream position x_{out} and the interior of both walls. With α denoting the angle between the deflected wall and the horizontal, the individual forces are

$$F_{p,x} = \int_{bot}^{top} (P(x,y) - p_{ref})\,\mathrm{d}y, \quad F_{p,ramp} = \int_{in}^{out} (P(s) - p_{ref}) \sin\alpha(s)\,\mathrm{d}s,$$

$$F_{fric} = \int_{in}^{out} \tau_w \cos\alpha(s)\,\mathrm{d}s, \quad F_{visc} = \int_{bot}^{top} \frac{1}{Re}\frac{\mathrm{d}U}{\mathrm{d}x}\mathrm{d}y, \quad M_x = \int_{bot}^{top} \overline{u^{*2}}(x,y)\,\mathrm{d}y,$$

where u^* is the (unfiltered) instantaneous velocity. Here and in the remainder of the article we set $\rho = 1$. For the reference pressure, p_{ref}, we use the pressure at the lower end of the downstream face of the control volume. The pressure difference force and ramp force can be combined into a net force $F_{p,net} = F_{p,out} - F_{p,in} + F_{p,ramp}$ which expresses the net effect of pressure acting on the entire control volume. The force $F_{fric,w}$ is evaluated for both walls. The momentum flux M_x consists of three parts

$$M_x = \int U^2\,\mathrm{d}y + \int \overline{u^2}\,\mathrm{d}y + \int \overline{\tau}_{11}\,\mathrm{d}y.$$

Since the deviatoric SGS-stress τ_{11} is smaller than $2 \times 10^{-5} U_b^2$ it can be neglected in the force balance. The isotropic part of the SGS stress enters the balance through the pressure. We neglect F_{visc} since the term scales with $1/Re$ and $\partial U/\partial x \ll \partial U/\partial y$.

Computation of the force balance for experimental data requires some minor modifications such as interpolating between data points near the walls where measurements are scarce, and interpolation of c_p-values in x. We assume that the pressure varies linearly across the duct in the experiments. The c_p-difference between the wall and interior resulting from the variance $\overline{v^2}$ is on average -0.005 and has been neglected for the experiments. Computing the force balance for LES results using this approximation rather than the real pressure distribution leads to a residual of the order of $0.04\delta U_b^2$ in the rear part of the diffuser. The friction force for the experiments is computed using c_f from the LES. No c_f measurements were reported by Obi, and Buice's measurements are too few to allow for meaningful integration of $c_f(x)$ along the walls. However, the error introduced by this assumption is small since skin friction data from the simulation follows closely the measurements of Buice (figure 8) and the overall contribution to the momentum balance is less than 5% of the momentum flux difference between the two control volume faces.

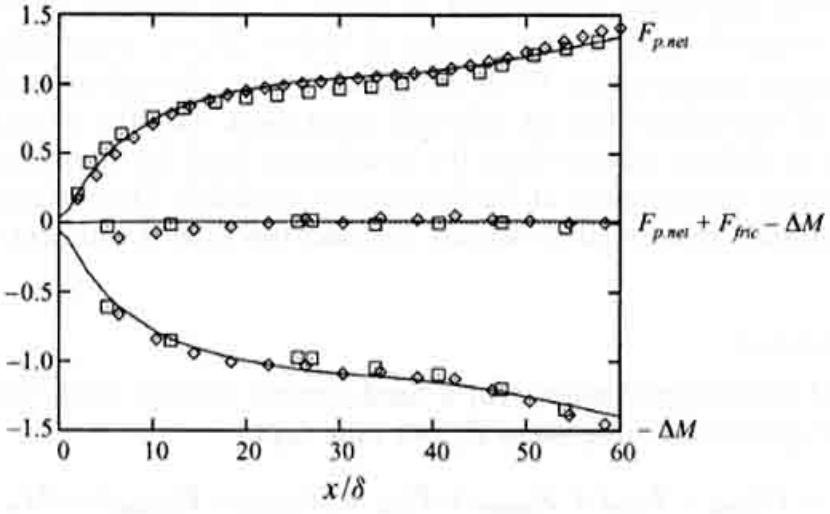

FIGURE 4. Individual terms contributing to the force balance for LES (case FINE ———), Obi (◇) and Buice (□). Momentum flux difference $-\Delta M = -(M_{in} - M_{out})$ (lower curves), residual $F_{p,net} + F_{fric} - \Delta M$ (middle) and net pressure force $F_{p,net}$ (upper curves) are normalized by δU_b^2.

Figure 4 depicts individual terms and the residual of the force balance for both experiments and simulation. The residual is less than 1% of the momentum flux difference for LES results, thereby validating the internal consistency of the simulation method and the force balance evaluation. Since friction contributes less than 5% to the momentum balance the flux difference ΔM is mainly balanced by the net effect of pressure with $F_{p,ramp}$ contributing about one third of the net pressure force.

The maximum residual for Buice's data set is $0.027\delta U_b^2$ which is below 1.5% of the incoming momentum flux. This accuracy is remarkable considering the approximations involved. We found it to be crucial to use the raw data, i.e. velocity measurements which were not scaled to satisfy global mass conservation, in order to obtain a small residual for Buice's data. Obi's data develop a higher residual which changes from negative to positive values with streamwise location x/δ. The positive values of the residual might come from neglecting the pressure variation across the duct. Another source for a larger force balance residual compared to Buice's data might be the use of scaled velocity data.

Although the primary purpose of the force balance is a check for the consistency of the experimental data we have also included simulation results in figure 4. Since LES and the experiments have nearly identical incoming momentum flux, the difference ΔM indicates how much outgoing momentum fluxes differ at the downstream face of the control volume. LES and Obi's data agree well whereas M_{out} is slightly higher for Buice in the region $20 < x/\delta < 30$, leading to a reduction in ΔM. Lower ΔM in Buice's data corresponds to a smaller net pressure force compared to the simulation and Obi downstream of $x/\delta = 20$. Note that the enhanced momentum flux is consistent with the slight flow-rate increase in Buice's experiment near $x/\delta = 25$. Since LES and Obi have similar c_p-curves (figure 8) the net pressure force can be expected to be close.

Overall, both experimental data sets satisfy mass and momentum balances for a nominally two-dimensional flow within acceptable error bounds which makes them well suited for validation of our computational study. Because of the significant mass balance residual in the tail duct, it is not recommended to use Obi's data downstream of $x/\delta = 40$.

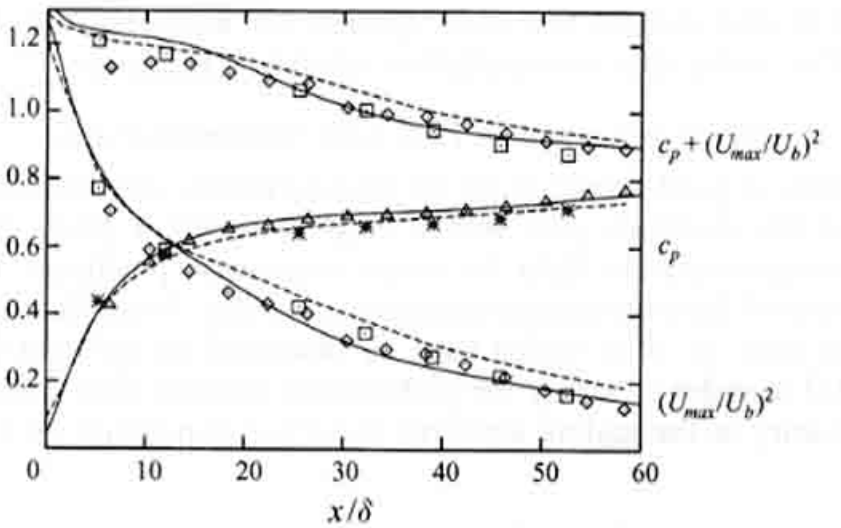

FIGURE 5. Depicted are c_p (lower curves), $(U_{max}/U_b)^2$ (middle) and total pressure $c_p + (U_{max}/U_b)^2$ (upper curves) for LES (case FINE ———), Durbin's RANS simulation (– – – –) and experiments of Obi (◇, △) and Buice (□, *).

3.1.4. *Consistency check using Bernoulli's equation*

As a consequence of conservation of energy the total pressure $c_p + (U/U_b)^2$ remains constant along a stream-tube in an incompressible, inviscid flow. A similar relation holds in a viscous flow such as the diffuser, with the important difference that the total pressure will in general decrease in the streamwise direction as a result of frictional losses. A generalized Bernoulli equation of the latter form is useful in the present case since it still illustrates the basic exchange between kinetic energy and pressure. We shall use it here to draw a connection between c_p along the upper wall and the peak value of the streamwise component U at any fixed streamwise station. Figure 5 reveals that viscous losses are significant in the diffuser, resulting in a 30% decrease in total pressure over the length of the domain. Included in figure 5 are data from a RANS computation by Durbin (1994). We find that computations and measurements exhibit about the same total pressure with the exception of Obi's data which fall short by about 5% of the total pressure upstream of $x/\delta = 15$. We attribute this deviation to the fact that raw data had been scaled to satisfy global mass balance.

Up to $x/\delta = 15$, LES and Durbin's RANS simulation predict larger U_{max} than the experiments. Further downstream Durbin's U_{max} exceeds that from the LES significantly. This translates into a lower c_p as compared to LES although the c_p-difference is much smaller than the difference in U_{max}^2. Here, the limitations of the Bernoulli relation for the present configuration become evident. Still, the deviation in c_p between LES and Obi on one side and Buice on the other side is consistent with the larger values of U_{max} found near $x/\delta = 25$ in Buice's data. There, the flow rate was about 5% higher than in the inlet duct which might explain the larger U_{max}.

Although the relationship between the pressure and velocity is not as direct as in an inviscid flow, the basic Bernoulli effect is still useful in interpreting some of the results which will be shown in the following sections. Since the relation between peak velocity U_{max} and pressure is essentially quadratic, a seemingly small mismatch in mean flow profile, for example, by 3%, translates into a c_p-difference of 6%. This fact highlights a major difficulty in accurate quantitative prediction of this flow. If, for example, through the presence of secondary flow additional mass flow is added to a region where the profile is peaked, even a small fraction of the total flow rate is sufficient to increase U_{max} considerably, thereby changing the pressure coefficient

significantly. It is also evident that error bounds for measurements of U_{max} have to be rather small to make data sets useful for validation purposes.

3.2. *Comparison of LES with experimental data*

In order to allow a good comparison of measurements and simulation results, we have combined the available data into a single plot for a given quantity, thereby occasionally interpolating the data for some streamwise positions. These plots also allow comparison of the experiments against each other. From Buice & Eaton (1997) we use the raw data, i.e. data scaled with U_b measured in the inlet duct. Obi's data have been scaled in order to satisfy the global mass balance. One should keep in mind that the uncertainty in the scaling amounts to 15% downstream of $x/\delta = 40$ for this data set.

3.2.1. *Comparison of mean flow and pressure recovery*

In figures 6 and 7 we compare profiles of mean streamwise velocity U, r.m.s. velocity fluctuations and turbulent shear stress $\overline{uv}$ from simulation and experiments in the first half and the rear part of the diffuser respectively. Results from simulations obtained on different grids (cases FINE and MED-W) are included. For the validation discussed in this section we restrict ourself to the data from case FINE. The effect of resolution on the results will be discussed in § 4.1.

Overall, the agreement of mean flow profiles between simulation and experiments is quite good. Upstream of $x/\delta = 10$ the peak velocity U_{max} of the simulation is slightly higher than in the measurements. This deviation is within the experimental error margin. Between $x/\delta = 25$ and $x/\delta = 35$ the situation is reversed, i.e. measurements exhibit slightly higher peak velocities U_{max} than the simulation. Note that Buice's profiles have not been scaled to conserve mass which explains the deviation at $x/\delta = 25$ where the flow rate is 5% too high.

The amount of backflow as well as the location and height of the separation bubble agree well up to $x/\delta = 55$. Reattachment and recovery occur further downstream in the simulation compared to the experiment. This translates into a mean bubble length of 53δ in the simulation compared to 47δ in Buice's experiment. Skin friction along both walls agrees well with Buice's measurements, see figure 8. Near the diffuser throat the mean flow detaches over a very short distance, indicated by c_f dropping to zero near $x/\delta = 2$ on the deflected wall. There, a very thin zone of backflow buried in the viscous layer exists which is completely disconnected from the separation bubble which begins at $x/\delta = 12.1$ and extends into the tail duct. Buice determined the location of vanishing wall stress using a thermal tuft to be at $x/\delta = 12$. The location of zero crossing in c_f is reached at a shallow angle. Accurate prediction of the exact location of vanishing shear stress is probably less important than of the overall shape of mean flow profiles and the slope of $c_f(x)$. Asymptotically, c_f (normalized by U_b of the incoming flow) in the tail duct will reach $1/a^2 = 0.045$ of the value found in the inlet duct. At $x/\delta = 70$, c_f on the flat wall is still twice as high as the value corresponding to equilibrium channel flow.

Most of the pressure increase occurs within the first third of the expansion with the steepest rise close to $x/\delta = 2$, see figure 8. Up to $x/\delta = 10$ the c_p-curves from LES and both experiments agree reasonably, with Buice predicting a slightly faster rise than Obi. Further downstream, LES and Obi agree well whereas Buice's data are about 5% lower in pressure recovery. All three curves exhibit a characteristic plateau in the region of the separation bubble.

It is not obvious why Buice's data deviate from Obi and LES. As explained in § 3.1.1,

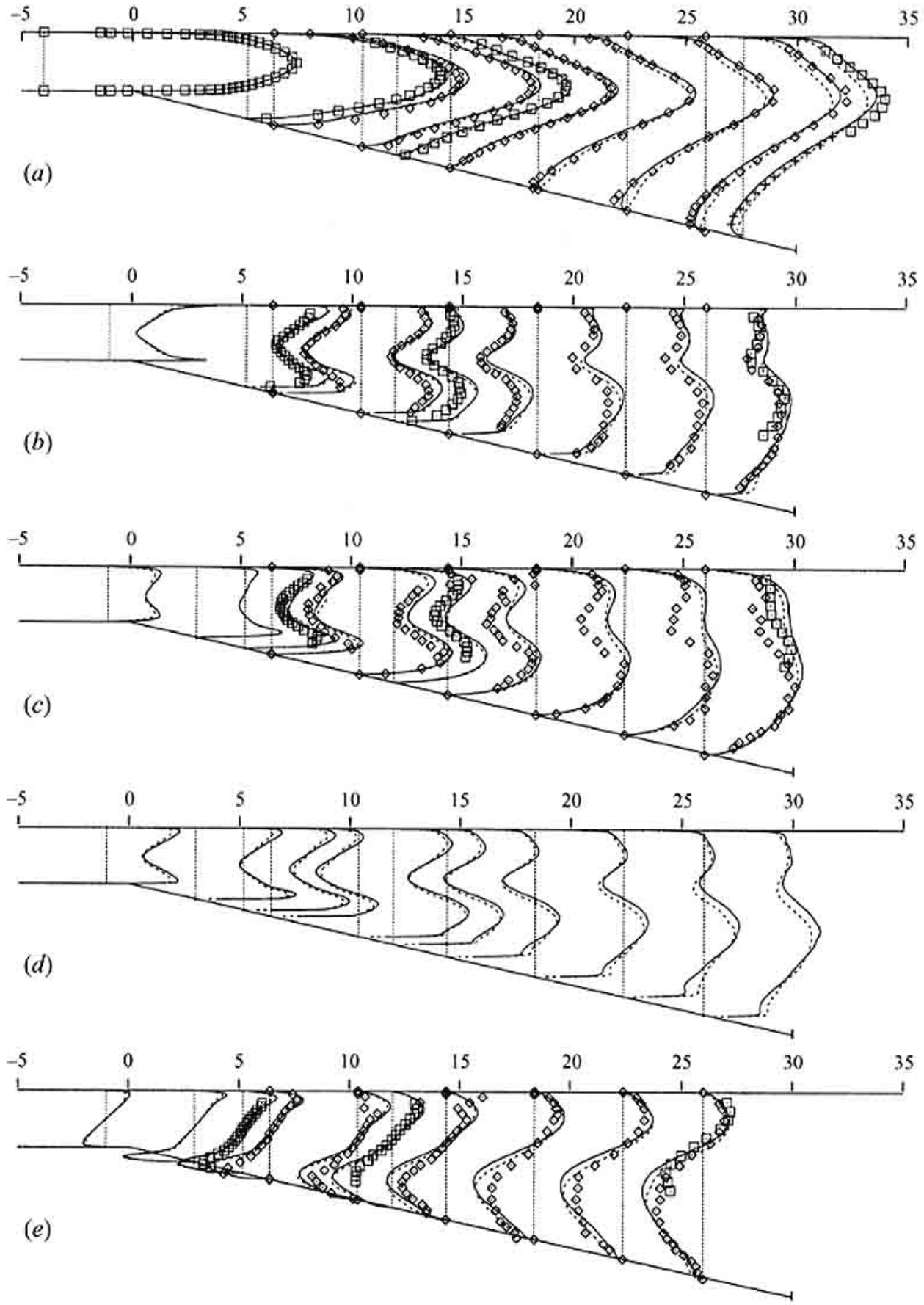

FIGURE 6. (*a*) Mean velocity $x/\delta + 10 \times U/U_b$; and r.m.s. velocity fluctuations: (*b*) $x/\delta + 30 \times u_{rms}/U_b$, (*c*) $x/\delta + 50 \times v_{rms}/U_b$, (*d*) $x/\delta + 50 \times w_{rms}/U_b$, (*e*) $x/\delta + 500 \times \overline{uv}/U_b^2$ in the first half of the diffuser. Line code: case FINE (———), case MED-W (– – – –), Obi (◇), Buice (□ single wire, + pulsed wire).

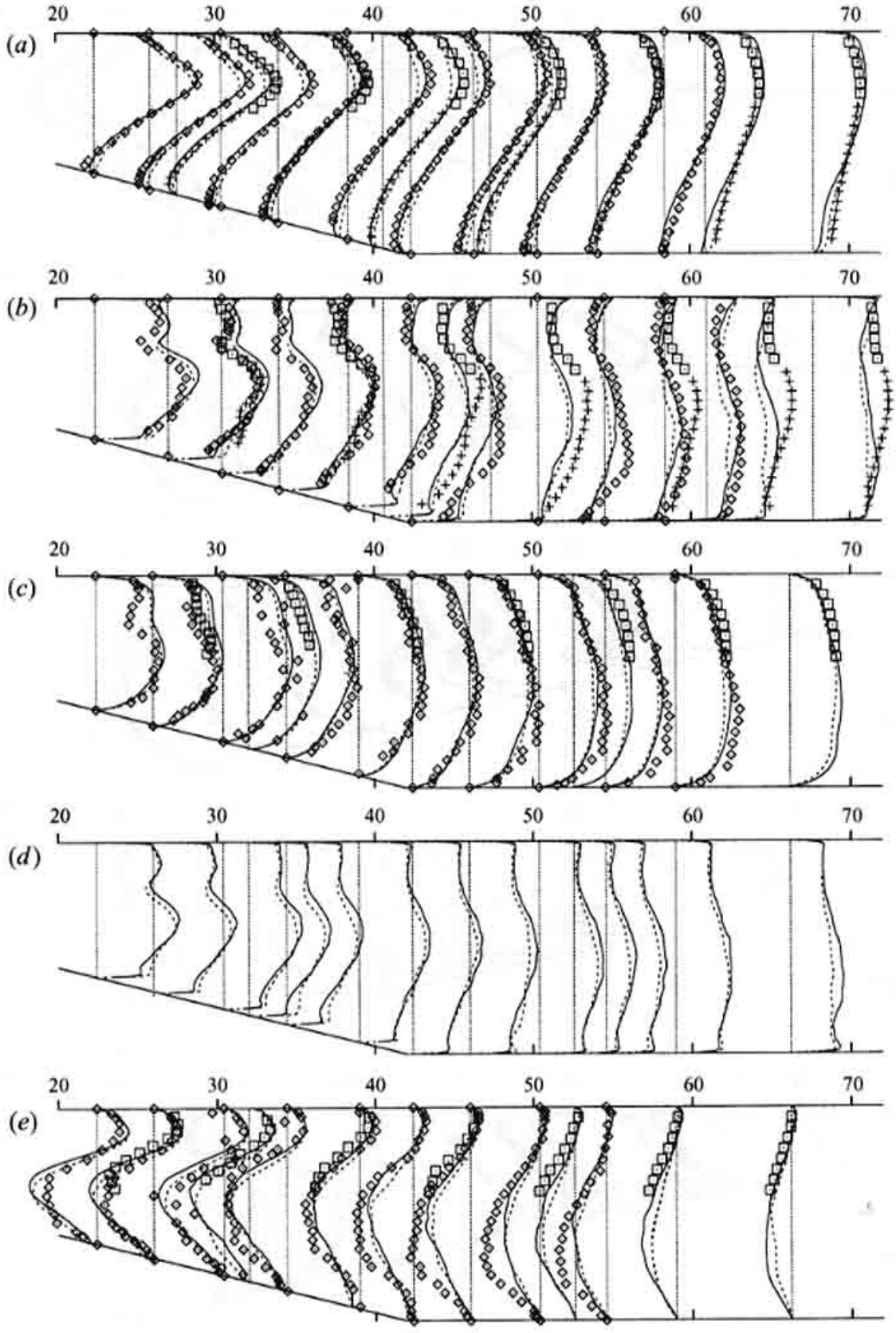

FIGURE 7. (a) Mean velocity $x/\delta+10\times U/U_b$; and r.m.s. velocity fluctuations: (b) $x/\delta+50\times u_{rms}/U_b$, (c) $x/\delta+50\times v_{rms}/U_b$, (d) $x/\delta+50\times w_{rms}/U_b$, (e) $x/\delta+750\times\overline{uv}/U_b^2$ in rear part of the diffuser. Line code: case FINE (———), case MED-W (– – – –), Obi (◇), Buice (□ single wire, + pulsed wire).

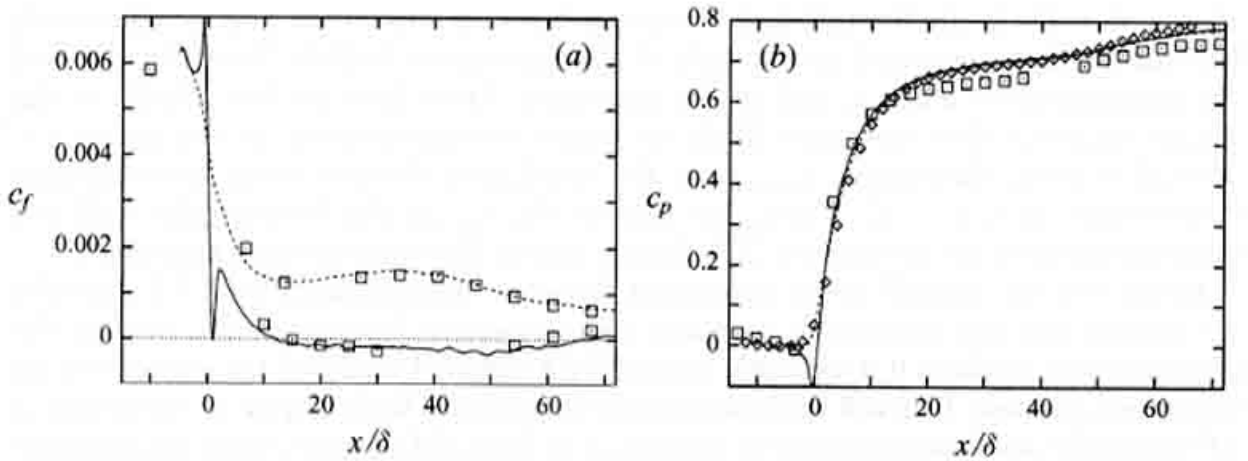

FIGURE 8. (*a*) Skin friction coefficient c_f based on U_b along deflected wall (———) and flat wall (– – – –) from LES (case FINE) and Buice (□). (*b*) Pressure coefficient c_p based on U_b: LES (case FINE) flat wall (– – – –), LES deflected wall (———), Buice deflected wall (□) and Obi flat wall (◇).

some uncertainty remains with respect to proper normalization of Obi's data. Using $U_{ref}/U_{bulk} = 1.14$ would result in 5% lower c_p for Obi. Although this scaling would give a similar pressure recovery of $\Delta c_p \approx 0.75$ in both experiments, it would produce a significant discrepancy in $c_p(x)$ upstream of $x/\delta = 10$. Additionally, residuals in the momentum balance for Obi would increase and the total pressure $c_p + (U_{max}/U_b)^2$ would deviate considerably from LES and Buice if this scaling were applied. We therefore conclude that c_p, as depicted in figure 8, is appropriate for comparison with our results.

A possible explanation for the 5% lower c_p in Buice's experiment lies in the observed mass flow increase in the middle section of the expansion. This excess mass might be a result of weak secondary flow or inhomogeneity in the span. In accordance with the Bernoulli relation we expect c_p to be lower in the region where U_{max} from Buice exceeds the LES value.

3.2.2. *Comparison of Reynolds stresses*

Measurement errors are higher for fluctuations than the mean flow, especially at the early stations where measurement volumes are large compared to the local gradients of r.m.s. profiles. Buice's measurements of u_{rms} are flawed near walls where the peak r.m.s. values are under-predicted by 10–20%. Measurements of v_{rms} are available only for regions where turbulence levels remained below 35%. Therefore, only partial profiles are shown in the rear part of the diffuser. A few profiles from LES upstream of the measurement stations are shown. A more detailed description of the flow in the entrance zone is given in § 5.1. The scatter among the two experiments is larger for r.m.s. values and shear stress than for the mean flow. Still, the agreement between the two datasets is good as can be seen at stations $x/\delta = 27, 34, 38$ where data from both experiments are available.

R.m.s. profiles from all three velocity components exhibit a characteristic shape with a double peak. The location of the peak value moves away from the wall into the flow interior with increasing distance from the diffuser throat. Locations of peaks for all three r.m.s. values are close to each other and coincide with the locations of peak values of $\overline{uv}$, which was also observed by Azad (1996) in a conical diffuser.

Profiles of u_{rms} from the simulation deviate from measurements upstream of $x/\delta = 25$. In this region the peak values of u_{rms} on the side of the deflected wall are 10–20% higher than in the experiments. A similar overshoot is observed for $-\overline{uv}$ in the region

$10 < x/\delta < 25$. Inside the tail duct deviations between simulation and measurements become more pronounced on the side of the separation bubble. Near the flat wall the agreements for u_{rms}, v_{rms} and $\overline{uv}$ are reasonable. Obi's data are less reliable in this region since the flow was most likely no longer two-dimensional in the mean. The vertical velocity fluctuation, v_{rms}, from the simulation deviates from measurements downstream of $x/\delta = 12$. There, the part of the v_{rms}-profile between flat wall and duct centreline is on average 10–20% higher in the LES than in the experiment.

Based on the overall good agreement between measurement and LES results, we believe that the simulation captures many essential features of the flow in this configuration, making it a valuable source for a detailed study of the physics of the separation process. This will be done in more detail in § 5. With respect to the ability of LES to make accurate quantitative prediction of Reynolds stresses some uncertainties remain. First, it is not clear to what degree the flow in the experiment might be influenced by the presence of secondary flow. A thorough validation requires more detailed measurements. In particular, more detailed measurements are needed in the entrance zone where the most severe changes to the turbulence occur and knowledge of the full Reynolds stress tensor is highly desirable. Ideally, measurements should include gradients of the Reynolds stresses to allow for local evaluation of the mean momentum balance.

4. Computational aspects of the simulation

The second step of validation involves testing the sensitivity of the simulation results with respect to several computational parameters such as domain size, grid resolution and inflow conditions. These tests are necessary requirements to assess whether the computational results represent a converged solution.

4.1. *Dependence on grid resolution*

For the present configuration the questions of adequate resolution and proper inflow conditions are closely coupled. Previous work has shown that *wall-resolving* LES, i.e. resolving the scales of motion which control the near-wall dynamics, requires rather fine mesh spacing. The situation is complicated by the fact that minimum resolution requirements for simulation of turbulent channel flow (at the inlet) depend on the specific numerical method. LES based on spectral methods has produced reliable results over a moderate Reynolds number range with near-wall spacing based on wall units of the order of $\Delta x^+ = 100$ and $\Delta z^+ = 30$ (Piomelli 1993; Kravchenko *et al.* 1996). The minimum spacing must be reduced by at least a factor of two in order to achieve results of comparable quality using second-order finite differences (Cabot 1994; Lund & Kaltenbach 1995). Thus, the quality of the inflow data entering the diffuser will depend on the resolution used to generate the inflow database.

It is less obvious what resolution is adequate inside the diffuser since turbulence structure changes strongly under the influence of adverse pressure gradient. In general one might expect grid requirements to become less severe since turbulence length scales are known to grow in a decelerating flow (Simpson 1989; Dengel & Fernholz 1990). Also, the mean shear decreases and turbulence production occurs farther away from the wall. It might well be that simulation of the flow inside the diffuser requires less resolution than a zero-pressure gradient flow of the same geometrical dimensions. Whether this is the case can be learned from systematic refinement studies. What complicates the situation is the fact that in our configuration – where spacing in the inlet duct and inflow generator are identical – grid refinement changes the upstream

inflow condition. It is difficult to predict in advance how sensitive the flow will be to upstream flow history. Since the turbulence changes drastically under an adverse pressure gradient, one might speculate that upstream effects are quickly forgotten. In this case, the separation process which occurs about one third distance into the expansion, might not depend much on the quality of the inflow data. On the other hand, experimental work by Dengel & Fernholz (1990) has shown that incipient separation from a smooth wall is very sensitive to small changes in the upstream pressure distribution. Again, only a systematic variation of the inflow condition will clarify this issue.

Ideally one would like to separate the effects of upstream flow history and grid resolution. This could be done by using inflow data created on a fine mesh and supplying the data after proper interpolation to the diffuser inlet plane using a coarser mesh for the diffuser domain. The fundamental idea of this procedure, which was used by Akselvoll & Moin (1995) in LES of a backward-facing step flow, is that the adverse effects of using too coarse a mesh in the inlet duct are not felt immediately beyond the inlet plane and that the desirable properties of the incoming flow such as mean flow profile shape will be conserved over a significant downstream distance. This technique was not used in the present study but it should be explored as a viable method for possible cost reduction.

Diffuser simulations were performed on grids as specified in table 1 in § 2.2. Results from the corresponding channel flow simulations are shown in figure 9. The wall-normal spacing with $\Delta y^+ = 1$ at the wall and the spanwise spacing $\Delta z^+ = 31$ were identical in channel simulations corresponding to cases FINE, MED-N, COARSE. The denomination of the cases refers to the *streamwise* spacing which was $\Delta x^+ = 100$, 50, and 31, respectively.

The channel flow results are converged in a statistical sense with respect to resolution in the wall-normal and the spanwise directions, i.e. further refinement in this direction – while the spacing is kept constant in the other directions – does not change the results. A channel simulation with $\Delta z^+ = 42$ (inflow for case MED-W) gave identical results as the simulation corresponding to MED-N despite slightly coarser resolution in the span.

The three channel simulations generating inflow for cases FINE, MED-N, COARSE differ with respect to the domain width. Comparing inflow simulations for cases MED-N and MED-W indicates that the domain width has negligible impact on the channel results, thereby corroborating that a 4δ domain is wide enough to properly describe the flow in the diffuser inlet duct.

Channel results were obtained with a hybrid code which employs identical spatial and temporal differentiation and SGS model to the code used for simulating the diffuser flow. On the finest mesh we used a time step $\Delta t = 0.002\delta/u_\tau$. Reduction of the streamwise spacing from 100 to 50 wall units drastically improves the shape and log-law intercept of mean velocity as well as fluctuation profiles. Further streamwise refinement down to $\Delta x^+ = 31$ is needed to establish the wake region in the mean flow profile. This is most evident in terms of the ratio of centreline to bulk velocity, U_c/U_b, which is 1.10, 1.12, and 1.14 in the three cases respectively; only the latter agrees well with the value measured in the inlet duct. On the finest mesh the cell aspect ratio is $\Delta x/\Delta z = 1$. Usually, the streamwise spacing is at least double the spanwise spacing (Piomelli 1993). Since we use a hybrid method with spectral accuracy in the spanwise direction, the streamwise spacing has to be relatively fine in order to compensate for errors from the second-order spatial approximation. Producing the same results with a pure finite volume code would require a factor 2 or 3 finer mesh

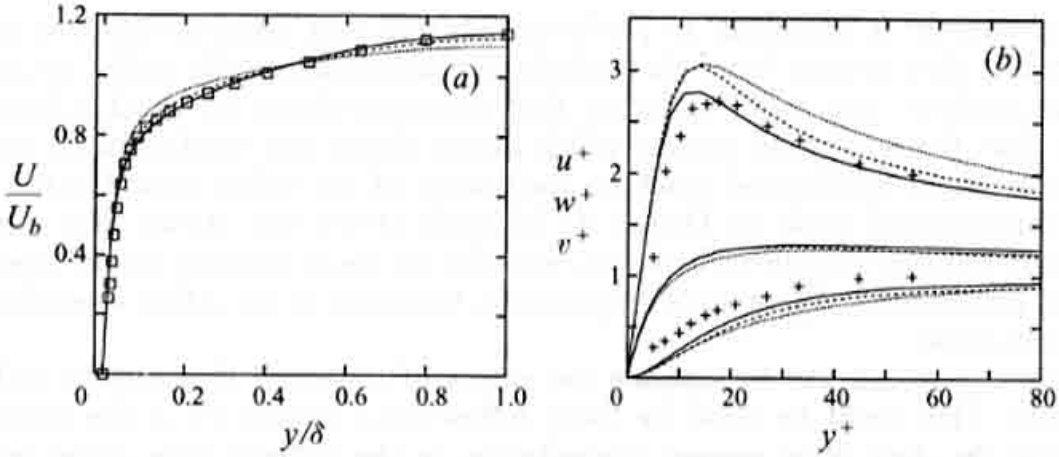

FIGURE 9. (*a*) Mean flow and (*b*) r.m.s. velocity fluctuations from turbulent channel flow at $Re_\tau = 500$ with streamwise spacing $\Delta x^+ = 100$ (·····), 50 (– – – –), and 31 (———); measurements: □ (Buice & Eaton 1997) and + (Wei & Willmarth 1989).

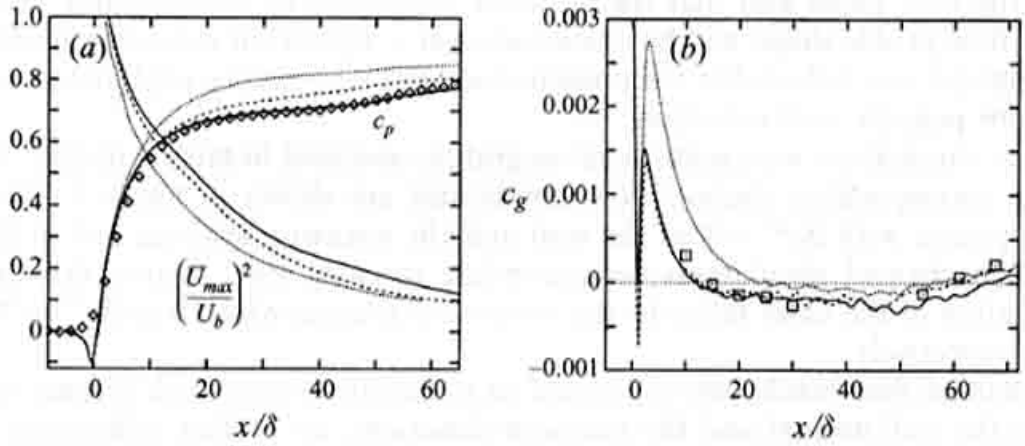

FIGURE 10. (*a*) Pressure coefficient c_p and peak velocity $\overline{U}^2_{max}$ and (*b*) skin friction along the deflected wall for cases COARSE (·····), MED-W (– – – –), FINE (———) and experiments by Obi (○) and Buice (□).

in the z-direction, thereby enhancing the cost significantly. Figure 10 compares the pressure coefficient and skin friction obtained from three simulations using different streamwise spacings as specified in table 1. For now we focus on the difference in resolution, postponing the discussion of domain width differences to the following section. We find a strong dependence of the simulation results on the quality of the inflow or – since they are connected – on the streamwise grid resolution provided in the inlet duct. As demonstrated in the previous section, the pressure coefficient is closely related to the peak of the mean velocity profile. Case COARSE under-predicts separation from the deflected wall, resulting in a c_p-difference of approximately 0.1 compared to the better resolved cases MED-W and FINE. Although the results further improve if we switch from medium to fine mesh, the change is not dramatic. Except for the tiny separation near the diffuser throat, skin friction on the inclined wall is almost identical on medium and fine mesh throughout the expansion.

In figures 6 and 7 we have plotted results from cases FINE and MED-W. These cases differ mainly with respect to the streamwise resolution in the inlet duct, and hence the quality of the inflow data. As stated above, the difference in spanwise resolution has negligible influence on flow evolution in the inlet duct. Inside the expansion, the streamwise spacing is almost identical for both cases. We therefore attribute the

improvement of the results mainly to the fact that the incoming flow has the correct ratio of $U_{cent}/U_{bulk} = 1.14$ on the finest mesh. The change in Reynolds stress profiles from medium to fine mesh is rather small. Upstream of $x/\delta = 15$ r.m.s.-profiles are nearly identical. Results from the two simulations are closer to each other than to the measurements. We do not observe a consistent trend for the stress profiles on the fine mesh being closer to experiments than the medium mesh case. In this sense we regard our results as being nearly grid-independent, i.e. further refinement is not likely to produce significant changes.

4.2. *Influence of domain width*

The spanwise mesh spacing is dictated by the requirements of the inlet duct as explained in the preceding Section. Since the simulation cost is proportional to the number of cells in the span it is desirable to choose L_z as small as possible without affecting the flow physics. Effects of domain width on numerical simulations of separated flows are discussed in Silveira-Neto *et al.* (1993) and Mittal & Balachandar (1997).

Because of the effect of wall blocking, the duct height h is the natural length scale which imposes a limit on the size of vertical spatial scales to be found in a duct flow. As long as turbulent motions are predominantly three-dimensional, spanwise scales will be limited by scales of the order of the duct height. In channel flows a domain width of approximately three duct heights is sufficient for the spanwise autocorrelation to drop to zero. However, even for domains as narrow as $L_z = 0.8h$ satisfactory results have been obtained (Piomelli 1993). Another example of a narrow domain in which the fundamental turbulence production mechanisms are captured is the minimal flow unit of Jimenez & Moin (1991).

Since the duct height varies with streamwise position in the diffuser the ratio of the width to height changes, with the smallest values found in the outlet duct. It can be expected that the constraint imposed by the spanwise domain size is felt gradually in the expanding section. For flows with mild separation it is known that the flow upstream of separation is generally unaffected by the conditions downstream (Simpson 1989). Masuda, Obi & Aoki (1994) found a similar behaviour in their diffuser experiment. Consistent with these observations are our own findings, namely that accurate simulations can be performed in a domain where the outflow boundary is chosen inside the expansion, for example at $x/\delta = 20$. Except for a region of approximately one local duct height upstream of the outflow boundary the upstream results were identical with a case simulated in the full domain.

Figure 11 compares pressure recovery and integral length scales from cases MED-N and MED-W with different domain widths and otherwise comparable parameters. Again, we emphasize that the 25% difference in spanwise resolution has no bearing on the following conclusions since statistics of the incoming flow are identical for both cases. The length scale $\ell_z = \int_0^{z_0} R_{ww}(z)\,\mathrm{d}z$ is derived from the spanwise autocorrelation of w, where z_0 denotes the location of the first zero crossing. Inside the inlet duct, ℓ_z from case MED-W is about 10% higher than for case MED-N. This difference indicates that a width of 4δ artificially limits the range of scales in the inlet channel of height 2δ, although – as stated before – mean flow profiles and turbulence statistics are identical for cases MED-N and MED-W upstream of the expansion. Integral length scales, ℓ_z, begin to differ substantially downstream of $x/\delta = 18$, i.e. in the region where the mean flow has separated. The domain width restriction causes the flow in case MED-N to separate more in the rear part and to re-attach more slowly compared to the wider domain case. This can be seen from the plateau in the c_p curve which

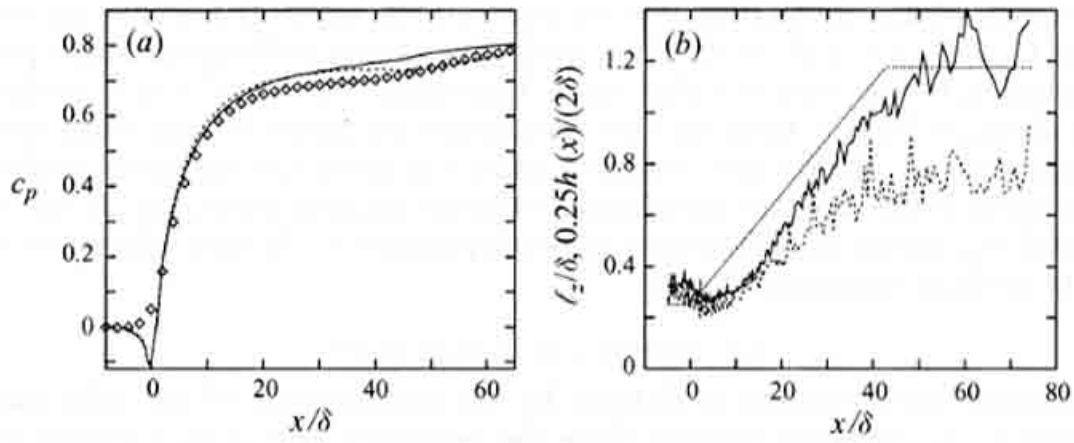

FIGURE 11. (*a*) Pressure coefficient c_p along deflected wall and (*b*) integral scale ℓ_z as a function of x/δ for domain of $L_z = 4\delta$ (MED-N – – – –) and 8δ (MED-W ——) and measurements from Obi (◇). The increase in diffuser cross-section $h(x)/(2\delta)$ is marked with ····· and has been scaled by a factor 0.25.

is typical for a flow with a shallow separation bubble. Clearly, a width of 4δ is too narrow for a reliable simulation of the entire diffuser flow.

Since the flow in the outlet duct will finally recover into a canonical channel flow we expect the ratio $\ell_z/h(x)$ to asymptotically reach the same value in the inlet and outlet ducts. From the geometry change alone a 4.7-fold increase in ℓ_z between the inlet and outlet ducts can be expected. It is interesting to compare the increase in length scale with the geometry change as depicted in figure 11. We find that the length-scale increase lags behind the geometry change and has not yet finished when the flow leaves the expansion and enters the tail duct. This is consistent with findings of Buice & Eaton (1997), that recovery into a developed flow takes places over a considerable distance downstream of the expansion.

There is a principal difficulty in defining spanwise scales in flows which exhibit significant coherence in the span such as bluff body wakes. Ideally, autocorrelations are computed after the phase-averaged mean has been removed from the signal. This is not possible in our case since no distinct oscillation at a single frequency is observed – although the diffuser exhibits low-frequency coherent motion in its downstream part (see § 5.2). We computed spanwise correlations from fields where the usual mean obtained from spanwise and time averaging was removed, see figure 12. The presence of significant spanwise coherence is responsible for the tails in the two-point correlations which do not drop to zero. The use of a wider domain would probably accelerate the breakup of the coherence in the spanwise direction.

An alternative way of exploring possible domain width influences is the examination of co-spectra $Co_{uv}(k_z)$. Co-spectra have been evaluated for case MED-W for several streamwise positions at the wall distances where $\overline{uv}$ profiles reach their maxima and minima, see figure 13. Clearly, the turbulent shear stress is carried by progressively larger scales with increasing distance within the expansion region. For most locations, the co-spectra reach their maxima inside the resolved wavenumber range, indicating that the momentum transfer is not severely hindered by a domain that is too narrow. This is the case along the flat wall. Along the deflected wall, the location of maximum $-\overline{uv}$ moves away from the wall towards the duct centreline, thereby getting contributions from larger scales. At $x/\delta = 50$ the peak in Co_{uv} has reached the lowest resolved mode, indicating that the domain is no longer wide enough. Based on these observations we have confidence in the domain independence of our results up to the

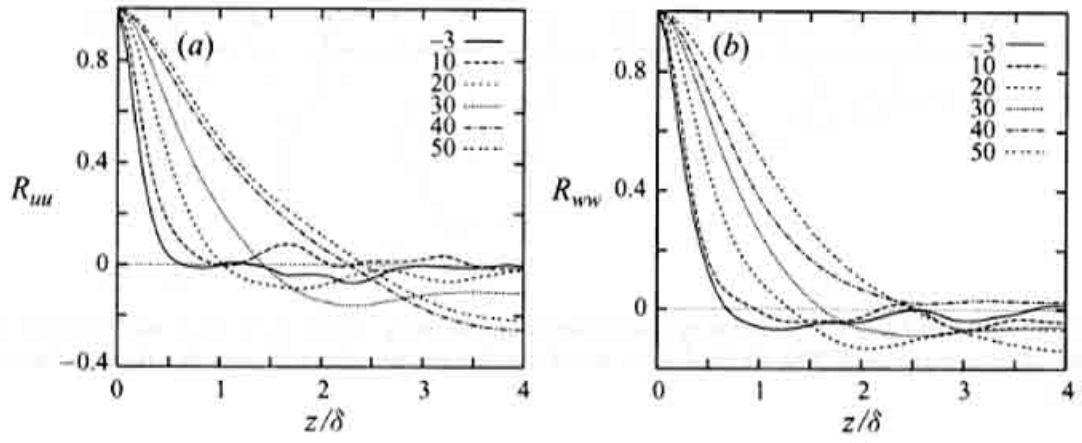

FIGURE 12. Spanwise autocorrelations (*a*) R_{uu} and (*b*) R_{ww} versus z/δ obtained at the centreline of the duct for case MED-W. The line coding identifies the streamwise position, x/δ.

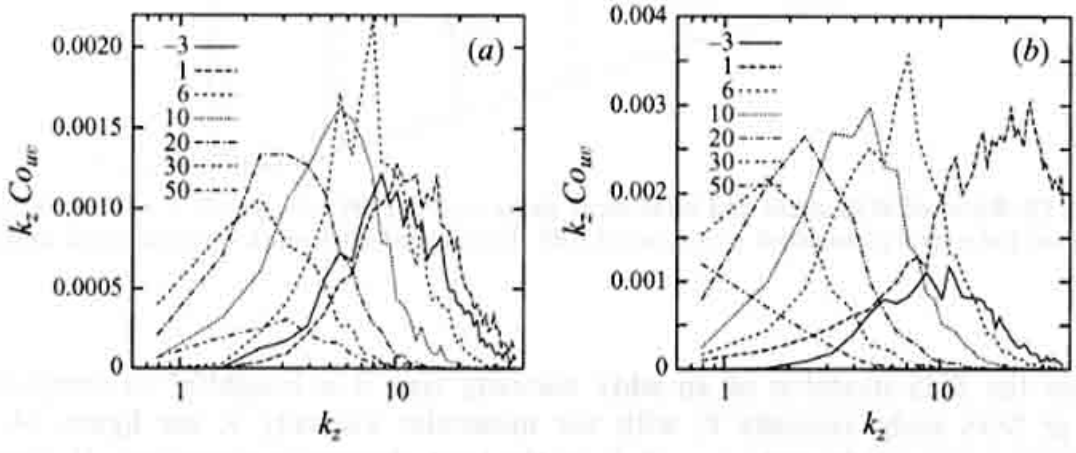

FIGURE 13. Co-spectra from case MED-W in semi-logarithmic, variance preserving form $k_z Co_{uv}$ versus $k_z = 2\pi n/L_z$ for locations of maximum (*a*) positive and (*b*) negative $\overline{uv}$, corresponding to flat and deflected walls respectively. For the deflected wall the sign has been reversed. The line coding identifies the streamwise position, x/δ.

end of the expansion, whereas the flow development in the tail duct is most likely influenced by box size limitations.

The domain size influence on length scale development and co-spectra has been documented for case MED-W. As we saw in the previous Section, case FINE predicts slightly more backflow than case MED-W, thereby agreeing better with the experiment except for the tail duct where reattachment is retarded. From the tendency observed on the medium mesh we conclude that further increase of the domain width for the fine mesh simulation might move the location of reattachment upstream.

4.3. *Role of the subgrid-scale model*

Since momentum transfer is predominantly a property of large scales, see figure 13, in LES the modelled stresses will always be a small fraction of the total shear stress. On the other hand, the fluctuating strain rate is most intense at small scales, providing the sink for kinetic energy. Hence, the SGS model affects primarily the energy budget rather than the momentum balance. In what follows we quantify the role of the SGS model in the present simulation by evaluating the SGS terms in the balances of mean momentum and turbulent kinetic energy.

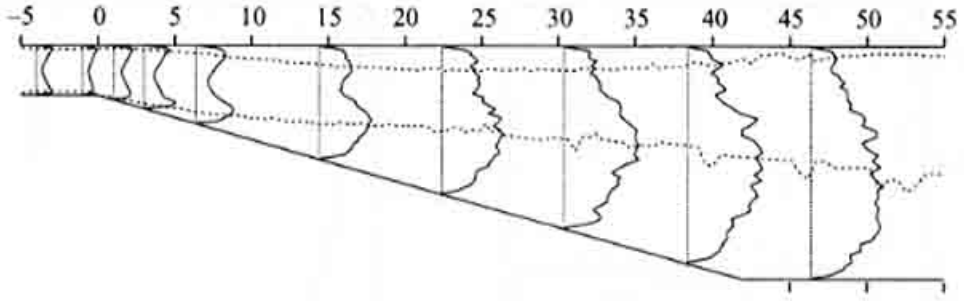

FIGURE 14. Ratio of SGS eddy viscosity and molecular viscosity: $x/\delta + \bar{\nu}_t/\nu$, i.e. 5 units on the x-axis correspond to a ratio of 5. The dashed lines mark the locations where $\overline{uv}$ reaches its maximum and minimum.

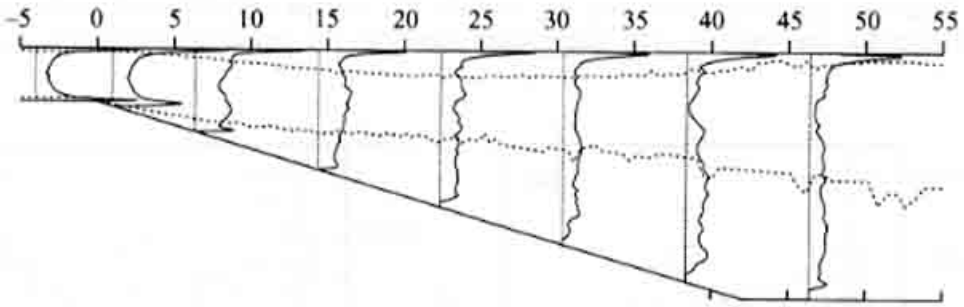

FIGURE 15. Ratio of SGS stress and total shear stress: $x/\delta + (100 \times \tau_{12})/(-\overline{uv} + \nu dU/dy + \tau_{12})$, i.e. 5 units on the x-axis correspond to a ratio of 0.05. The dashed lines mark minimum and maximum of $\overline{uv}$.

Since the SGS model is of an eddy viscosity type it is insightful to compare the average SGS eddy viscosity $\bar{\nu}_t$ with the molecular viscosity ν, see figure 14. The maximum value of the ratio $r_\nu = \bar{\nu}_t/\nu$ in the inlet channel is about one. It increases monotonically with downstream distance from the diffuser throat and reaches a maximum value around 6 in the outlet duct. Except for a small region along the curved wall the maxima of r_ν are found close to the peak locations of $\overline{uv}$. Along the deflected wall these locations correspond approximately to where the mean flow profiles have inflection points, and the mean shear reaches a (local) maximum. Since the mean shear contributes strongly to the strain rate it can be expected that the SGS viscosity becomes large in this region.

Large values of $\bar{\nu}_t$ do not necessarily imply that SGS stresses play a significant role in the momentum balance. We assess the model influence on the mean momentum by computing the ratio of SGS stress τ_{12} and total stress $-\overline{uv} + \nu dU/dy + \tau_{12}$ as shown in figure 15. Peak values of the stress ratio of the order of 8% are found close to both walls in the inlet channel and along the flat wall where the flow is attached. Apart from a thin layer along the flat wall the contribution of τ_{12} remains below 2% of the total stress downstream of $x/\delta = 10$. Therefore, the model influence on the mean momentum decreases towards the diffuser outlet – despite the significant increase in SGS eddy viscosity.

Additional support for the finding that the SGS model becomes less important for momentum transport with increasing downstream distance comes from inspection of the spectra of turbulence fluctuations. Spanwise spectra of both streamwise and vertical fluctuations exhibit peaks which move to lower wavenumbers with increasing distance from the diffuser throat, see figure 16. In the inlet channel as well as near the diffuser throat the spanwise spacing is adequate to resolve the most energetic

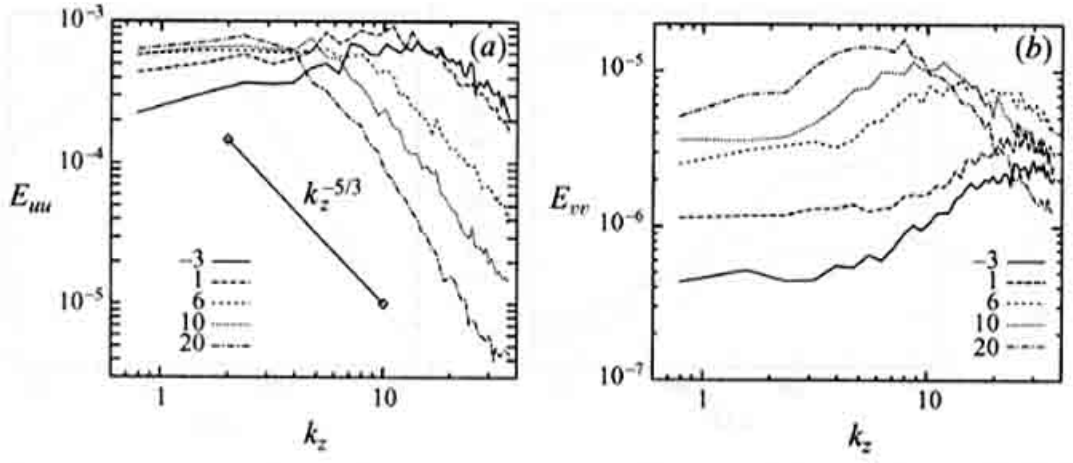

FIGURE 16. Spectra of (*a*) streamwise and (*b*) vertical velocity fluctuations from case MED-W at approximately 0.02δ or $y^+ = 10$ along the flat wall versus wavenumber $k_z = 2\pi n/L_z$. The line coding denotes streamwise position in x/δ.

motions near the wall. It is evident that the mesh could be considerably coarsened in the spanwise direction downstream of $x/\delta = 6$ without affecting the range of scales which carries the major part of the kinetic energy. Up to $x/\delta = 10$, the slope of the high-wavenumber end of the spectra is close to $-5/3$ and slightly steeper further downstream. At this low Reynolds number we do not expect an extended inertial subrange in the spectra. Nevertheless, our results are consistent with frequency spectra measured by Buice & Eaton (1997) in the interior of the diffuser at $y^+ \approx 300$), which exhibit a $-5/3$-power law decay over one decade.

In order to quantify the impact of the model on the level of the resolved turbulent kinetic energy $k = \frac{1}{2}\overline{u_i u_i}$ we examine the transport equation for k, i.e.

$$\frac{\partial(Uk)}{\partial x} + \frac{\partial(Vk)}{\partial y} = \frac{\partial F_1}{\partial x} + \frac{\partial F_2}{\partial y} - 2\,\overline{uv}\,S_{12} - \overline{u^2}S_{11} - \overline{v^2}S_{22} - \epsilon_{mol} - \epsilon_{SGS}. \tag{4.1}$$

Here, fluxes F_i are defined as $F_i = -\overline{pu_i} + (2/Re)\,\overline{u_j s_{ij}} - \overline{u_i(\frac{1}{2}u_k u_k)} - \overline{u_j \tau_{ij}}$, and $\epsilon_{SGS} = -\overline{\tau_{ij}s_{ij}}$ and $\epsilon_{mol} = (2/Re)\,\overline{s_{ij}s_{ij}}$ are SGS and molecular dissipation rate respectively. We recall that the only sink for k results from the fluctuating strain rate $s_{ij} = \frac{1}{2}(\partial u_i/\partial x_j + \partial u_j/\partial x_i)$. Part of the mean flow kinetic energy is dissipated directly by the mean strain rate $S_{ij} = \frac{1}{2}(\partial U_i/\partial x_j + \partial U_j/\partial x_i)$. Integration of (4.1) across the duct results in

$$\int_{bot}^{top} \frac{\partial(Uk)}{\partial x}\mathrm{d}y = \int_{bot}^{top} \frac{\partial F_1}{\partial x}\,\mathrm{d}y + \int_{bot}^{top} \mathscr{P}\,\mathrm{d}y - \int_{bot}^{top} \epsilon_{tot}\,\mathrm{d}y, \tag{4.2}$$

where $\mathscr{P}$ and ϵ_{tot} denote the production and dissipation terms respectively. From integration of (4.2) along the x-coordinate between stations x_{in} and x_{out} follows that the energy flux difference $\int_{bot}^{top}(Uk)_{out}\,\mathrm{d}y - \int_{bot}^{top}(Uk)_{in}\,\mathrm{d}y$ is a result of the streamwise accumulated imbalance of production and dissipation, i.e. $\int_{in}^{out}\int_{bot}^{top}(\mathscr{P} - \epsilon_{tot})\,\mathrm{d}x\,\mathrm{d}y$ plus the flux difference $(\int_{bot}^{top} F_{1,x_{out}}\mathrm{d}y - \int_{bot}^{top} F_{1,x_{in}}\mathrm{d}y)$, the latter term being small.

Figure 17 shows that the energy production nearly triples in a very short region at the beginning of the expansion. It peaks at $x/\delta = 2$ and drops monotonically to below 25% of the value found in the inlet channel. The sharp increase in production results mainly from the enhanced turbulent shear stress near the deflected wall, see figure 6, rather than increased mean rate of strain. A similar observation was made by Stieglmeier *et al.* (1989) in an axisymmetric diffuser. Again, it is interesting to compare

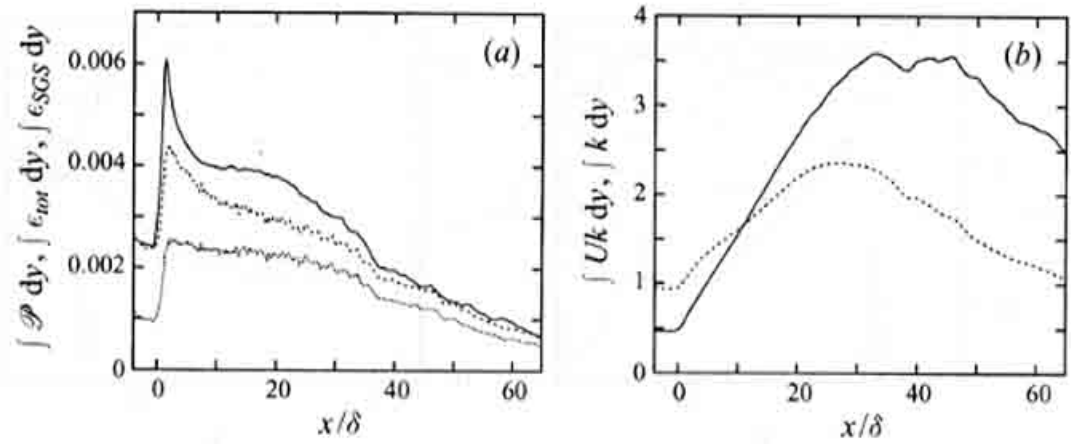

FIGURE 17. Terms of energy balance and kinetic energy integrated over the cross-section as a function of streamwise location. (*a*) $\int \mathscr{P}\,\mathrm{d}y$ (——), $\int \epsilon_{tot}\,\mathrm{d}y$ (- - - -), $\int \epsilon_{SGS}\,\mathrm{d}y$ (·····), normalized by U_b^3. (*b*) Energy flux $\int Uk\,\mathrm{d}y$ (- - - -) and kinetic energy $\int k\,\mathrm{d}y$ (——) normalized by the corresponding values at the inlet. The kinetic energy curve has been scaled by the factor 0.5.

the current value of the integrated energy production reached in the tail duct with the value to be reached asymptotically once the flow equilibrates. For equilibrium channel flow the energy production ratio (integrated across the duct and normalized by $U_{b,in}^3$) decreases with the third power of the area ratio, i.e. $\int \mathscr{P}_{in}\mathrm{d}y / \int \mathscr{P}_{out}\mathrm{d}y = a^3 = 103.8$. Thus, energy production will finally drop below 1% of the value in the inlet duct. Obviously, the flow in the tail duct is still far from the asymptotic state.

Inside the inlet channel energy is dissipated at the same rate as it is produced, i.e. the flow is in equilibrium. The strong increase in production near the diffuser throat is not matched by a corresponding increase in the total dissipation rate $\epsilon_{tot} = \epsilon_{SGS} + \epsilon_{mol}$. Production exceeds dissipation throughout most of the expansion, i.e. the flow is out of equilibrium. As a consequence, the energy flux $\int Uk\,\mathrm{d}y$ increases, the slope of the curve being controlled by the excess $\int (P - \epsilon_{tot})\mathrm{d}y$. Since the bulk velocity decreases inside the expansion, an increase in energy flux is achieved only when the energy itself grows at a faster rate than the duct height $h(x)$. Indeed, the area-weighted kinetic energy is about six times higher near the end of the expansion than in the inlet duct, see figure 17. The asymptotic value $\int k_{out}\mathrm{d}y / \int k_{in}\mathrm{d}y = 1/a = 0.21$. Thus, kinetic energy is away from equilibrium by a similar margin – namely an order of magnitude – away as energy production rate.

The SGS model responds to the increase in turbulent kinetic energy by enhancing the SGS dissipation rate. Downstream of $x/\delta = 10$ more than 80% of the total energy dissipation rate is provided by the SGS model. This rather large contribution is in contrast to the marginal impact of SGS terms on the momentum level. The present example shows the importance of the SGS model for regulation of the energy budget in a non-equilibrium flow.

In §3.2 we compared r.m.s.-values $u_{i,rms}$ from the simulations and experiments without accounting for SGS contributions. Based on the assumption of the existence of an inertial subrange with locally isotropic turbulence the SGS kinetic energy can be estimated from the SGS eddy viscosity as $k_{SGS} = (\nu_t/(0.0856\Delta))^2$ (Schmidt & Schumann 1989). The ratio k_{SGS}/k reaches maximum values of about 4% near $x/\delta = 3$ and decreases to less than 1% towards the outlet duct. Therefore, neglecting SGS stresses has little impact on the comparison of Reynolds stresses from simulation and unfiltered experimental data.

5. Flow physics

We aim at demonstrating what kind of information can be extracted from the simulation database, how it can be used to obtain deeper insight into flow physics, and how this information might be used for turbulence modelling. In the following we focus on two aspects of the diffuser flow: details of the flow in the diffuser entrance are presented first and subsequently some insight is provided into the unsteady separation process which takes place in the rear part.

5.1. *Flow in the entrance section*

The flow in the vicinity of the diffuser throat has several features which warrant a detailed study. The major part of the pressure rise occurs upstream of $x/\delta = 10$ with the maximum adverse pressure gradient found at $x/\delta = 1.8$. Since the diffuser is asymmetric, the flow developments are very different along the two walls. We will compare the corresponding mean flow and turbulence statistics and make an attempt to explain the differences on both walls in terms of pressure and strain history. Since our computation gives detailed information on the state of turbulence as well as its production mechanism, we are able to make precise statements about locations where geometrical changes are likely to have large effects. This information might be of use in the design of devices built to obtain maximum pressure recovery.

Unfortunately, no experimental data are available near the diffuser throat upstream of $x/\delta = 5$. There, turbulence stresses change rapidly over short distances and small measurement volumes are needed to correctly capture these changes. Our results show that the flow field in the throat is very complex with turbulence being influenced by rapid changes in pressure, curvature and strain. With the lack of direct measurements in this region we can only indirectly conclude how reliable our computational results are. Since simulation results for mean flow and turbulence statistics agree well with measurements inside the inlet duct ahead of the throat and inside the expansion downstream of the throat we are confident that the simulation gives a realistic description of the flow physics in the entrance zone.

Figure 18(*a*) depicts the pressure along both walls. Streamwise and radial pressure gradients are plotted in figure 18(*c*). In order to follow the deflected wall, the flow must turn which causes a radial pressure gradient between $-2 < x/\delta < 2$. The maximum pressure difference between both walls is $\Delta c_p = 0.11$, i.e. about 14% of the overall pressure rise. The magnitude of the radial pressure gradient is comparable to the adverse pressure gradient (APG).

Whereas the pressure rises monotonically along the flat wall a 'suction peak' develops on the curved part of the deflected wall. There, the magnitude of the maximum favourable pressure gradient is about one half of the maximum APG. The maximum APG on the deflected wall is about twice as strong as on the flat wall. The strength of the APG can be characterized by the Clauser parameter $(\delta^*/\tau_w)\mathrm{d}p/\mathrm{d}x$. Along the flat wall it is about 3 at $x/\delta = 2$ and reaches a peak value of 5.5 at $x/\delta = 10$.

The mean strain rate also undergoes rapid changes in the diffuser throat. Figure 19 shows the maximum eigenvalue λ_{max} of the strain rate tensor which corresponds to the principal axis direction of 45° with respect to the normal of the wall. Along the flat wall we find a monotonic decrease of the strain rate maximum by more than 50% over a distance of 5δ. This is mirrored in the decay of the skin friction depicted in figure 18(*b*). Downstream of $x/\delta = 0.5$ the strain rate maximum no longer occurs at the wall but rather a short distance into the flow interior.

Along the deflected wall, the streamwise strain history is very different. Due to the

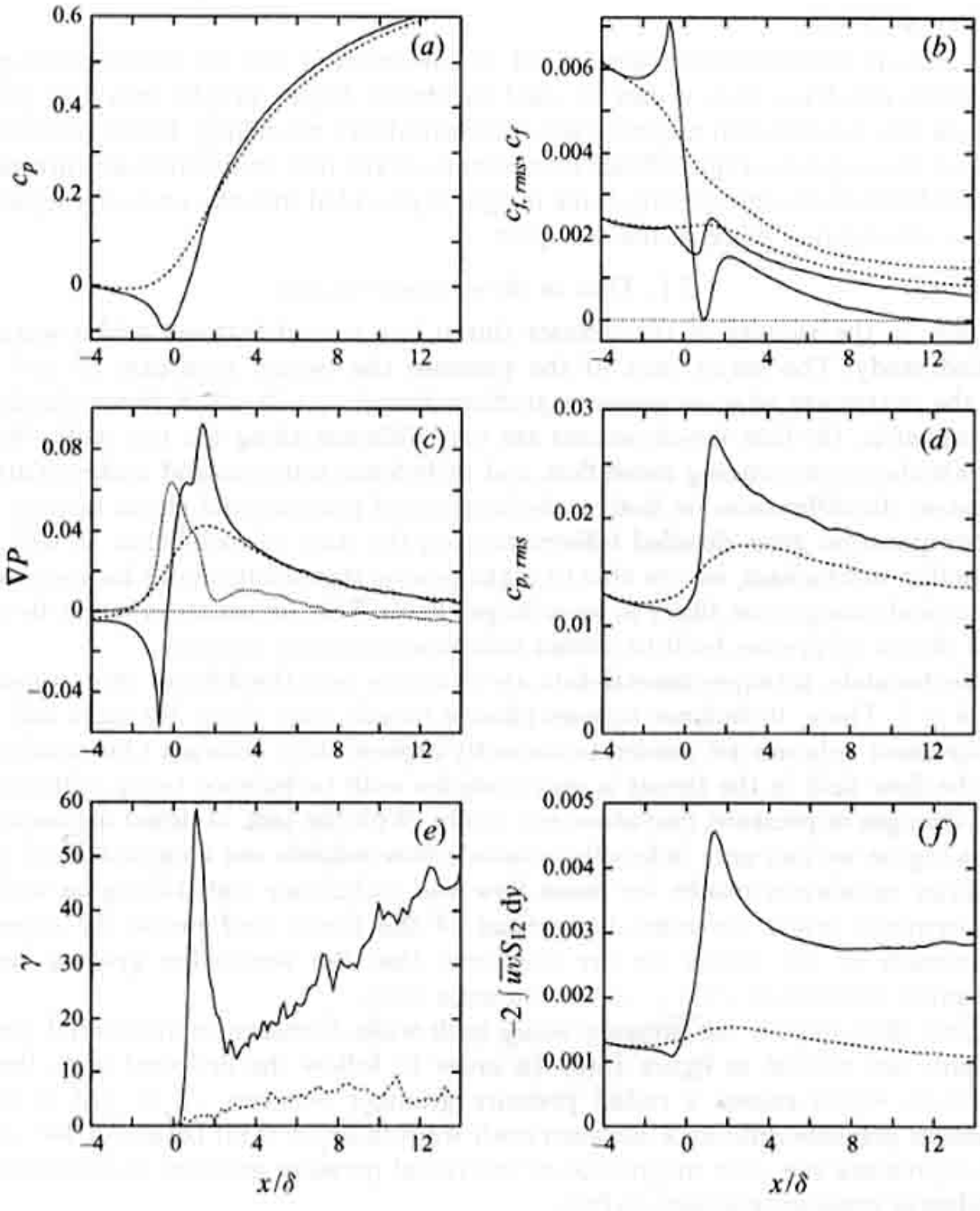

FIGURE 18. Flow details in the entrance section along the deflected (———) and flat (– – – –) wall: (*a*) pressure coefficient c_p, (*b*) mean skin friction c_f (intercepts at 0.006) and fluctuations $c_{f,rms}$ (intercepts at 0.0024), (*c*) streamwise pressure gradients along both walls and radial pressure gradient along a streamline starting at $y/\delta = 0.2$ (·····), (*d*) fluctuating wall pressure $c_{p,rms}$, (*e*) reverse flow fraction γ in percent, (*f*) production $-2\overline{uv}S_{12}$ integrated from each wall up to the location of U_{max}.

favourable pressure gradient the peak strain rate or skin friction is initially about 15% higher than on the flat wall. Near $x/\delta = 0.1$ the strain rate peak moves away from the wall into the flow interior. It decreases at a faster rate than on the flat wall, reaching about 4 at $x/\delta = 1$ compared to 8.3 at the upper wall. Whereas high strain rate is concentrated in a narrow layer along the flat wall we observe appreciable values as far as 0.1δ away from the deflected wall. Downstream of $x/\delta = 1$ the near-wall peak in the strain rate profile normal to the deflected wall redevelops which leads to an increase of strain rate magnitude over a short streamwise distance. This is remarkable in that the strain rate increase occurs despite the adverse pressure gradient. Usually,

flow deceleration due to an APG leads to a reduction of the strain rate as is the case along the flat wall.

Streamwise changes of pressure and skin friction are closely coupled. As a result of the strong APG the skin friction drops below zero for a very short region near $x/\delta = 1.2$ on the deflected wall. This small separation zone is buried in the viscous layer and is well upstream of the mean separation bubble near $x/\delta = 12$ which extends into the tail duct. Instantaneous backflow occurs along both walls as early as $x/\delta = 0.3$, see figure 18(*e*). The reverse flow fraction γ stays briefly above 50% at the deflected wall before dropping to 15% at $x/\delta = 3$. Beyond this station it rises gradually and reaches 50% near the mean flow separation point at $x/\delta = 12.1$.

Instantaneous reverse flow on the upper wall remains below 10%. Interestingly, the maximum flow reversal fraction for the flat wall is far downstream of the location where the APG was maximum, whereas the peak APG on the deflected wall induces strong instantaneous backflow. The fact that instantaneous backflow occurs well ahead of the location of mean separation is a typical feature of flows with pressure-driven separation (Simpson 1989; Alving & Fernholz 1996; Na & Moin 1998). What is different in our case is the fact that the flow has separated and reattached on the deflected wall before it reaches the point where the large separation bubble forms. The flow reversal γ increases slowly downstream of $x/\delta = 3$, indicating that separation is a gradual process. As pointed out by Simpson (1989) it is questionable to distinguish individual flow zones such as 'separation bubble' and 'region of attached flow' based on mean flow topology. It is much more appropriate to describe the decelerating flow inside the expansion as a superposition of instantaneous flow states which range from being locally attached to temporarily separated.

The mean skin friction drops at a higher rate than the fluctuations $c_{f,rms}$ with increasing downstream distance from the diffuser throat, see figure 18(*b*). As a consequence the ratio $c_{f,rms}/c_f$ increases from 0.4 up to 0.8 near $x/\delta = 10$ along the flat wall. Except for the corner zone the skin friction fluctuations have comparable magnitudes along both walls. This is remarkable since mean flow and wall shear are so different. Apparently, near-wall turbulence in a flow approaching separation is not fundamentally different from a fully attached flow. This view is corroborated by the results of Na & Moin (1998) who found that the characteristic near-wall structure of a turbulent boundary layer with low- and high-speed streaks remains intact up to shortly ahead of the location of mean separation.

Another quantity which is of interest in engineering diffuser flows is the wall pressure fluctuations. Figure 18(*d*) shows the twofold increase of this quantity along the deflected wall. Peak values of p_{rms} are found at the location $x/\delta = 1.8$, where the APG reaches a maximum. Along with the drastic increase in wall pressure fluctuations we observe a rapid enhancement of turbulence production on the side of the deflected wall, see figure 18(*f*). Production of kinetic energy is symmetric in the inlet duct, and the threefold increase in production rate occurs almost exclusively on the side of the deflected wall. This asymmetry can also be be seen in profiles of v_{rms} and $\overline{uv}$ which show drastic differences in peak values on both walls. Most dramatic is the local fivefold increase in the maximum production rate $-\overline{uv}\mathrm{d}U/\mathrm{d}y$ which occurs over a streamwise distance of 1.5δ along the curved section of the throat. In contrast to the profiles of v_{rms}, $\overline{uv}$, and $-\overline{uv}\mathrm{d}U/\mathrm{d}y$, the profiles of u_{rms} and w_{rms} are nearly symmetric, i.e. peak r.m.s. values are similar near the flat and deflected walls.

These observations are consistent with the following scenario in which wall-normal velocity fluctuations play a crucial role due to several reasons. First, $\overline{v^2}$ is part of the production term in the budget of $\overline{uv}$. Secondly, wall-pressure fluctuations will be

enhanced in regions of enhanced wall-normal motion since the wall forces approaching fluid into wall-parallel directions. A possible explanation for the extreme asymmetric turbulence properties in the diffuser throat zone lies in the change of the surface normal with respect to the mean flow direction. The wall-normal motion inside the inlet duct is restricted through the presence of solid surfaces. As the flow enters the expansion it tends to maintain its original direction through inertia. This gives way to enhanced wall-normal motion on the side of the deflected wall whereas the geometrical restriction remains along the flat wall which prevents a similar mechanism increasing production near the wall. The fact that the rapid increase in turbulence production occurs near the wall suggests that the source is the sudden geometry change and not the pressure gradient. An adverse pressure gradient tends to decrease Reynolds stresses in the inner region and to shift stress peaks away from the wall (Alving & Fernholz 1996). This behaviour is also observed in our case but much further downstream.

So far, the discussion has been based on a Cartesian frame of reference. For model development it is more instructive to present results independent of the coordinate system. A good measure for changes in the Reynolds stress tensor is the second invariant of the anisotropy tensor $b_{ij} = \overline{u_i u_j}/q^2 - 1/3\delta_{ij}$, defined as $II = -0.5b^2$. It is zero in isotropic turbulence and 1/3 in a one-component state of turbulence. This quantity is plotted in figure 19(b,d) for regions close to both walls. In the inlet channel the maximum anisotropy is found at a distance 0.02δ or 10 wall units away from the wall. Along the flat wall the anisotropy decreases monotonically under the influence of the APG. At $x/\delta = 3.9$, the maximum value has been reduced to about 50% of its upstream value. We observe a very different behaviour along the deflected wall where the peak anisotropy increases slightly as the flow enters the diffuser throat. Once the APG has built up – around $x/\delta = 0.5$ – the maximum anisotropy decreases monotonically similarly to the flat wall. On the deflected wall, the location of maximum anisotropy moves further away from the wall compared to the flat wall. At $x/\delta = 1.5$ the maximum anisotropy is smaller on the deflected wall than on the flat wall but extends over a wider region into the flow interior. Only at $x/\delta = 3.9$ do the profiles of $-II$ begin to look qualitatively similar again along both walls.

The streamwise change in profiles of maximum strain rate eigenvalue and of second invariant of the anisotropy tensor look qualitatively similar. Along the flat wall, both quantities decay monotonically in the streamwise direction whereas on the deflected wall both profiles develop a broader peak moving away from the wall. From rapid distortion theory it is known that anisotropy state and mean strain rate are closely coupled. Therefore, the similarity in profile shapes indicates that turbulence undergoes changes a significant part of which is caused by linear interaction of the fluctuations with the mean strain field.

The mean strain field in turn is a result of the flow being subjected to strong pressure gradients. However, it appears useful to consider the strain history when discussing the flow development in this zone rather than to explain the changes solely in terms of pressure gradients.

Complex physics of the diffuser entrance poses a serious challenge for computation as well as modelling. There, changes in mean flow are rather small compared to the change in the turbulence energy budget as well as individual Reynolds stresses. This means that a thorough validation should definitely include comparison of computed (or modelled) stresses with measurements.

Our results can be used to evaluate predictions from RANS models which carry equations for the full Reynolds stress tensor. In particular, the capability of models

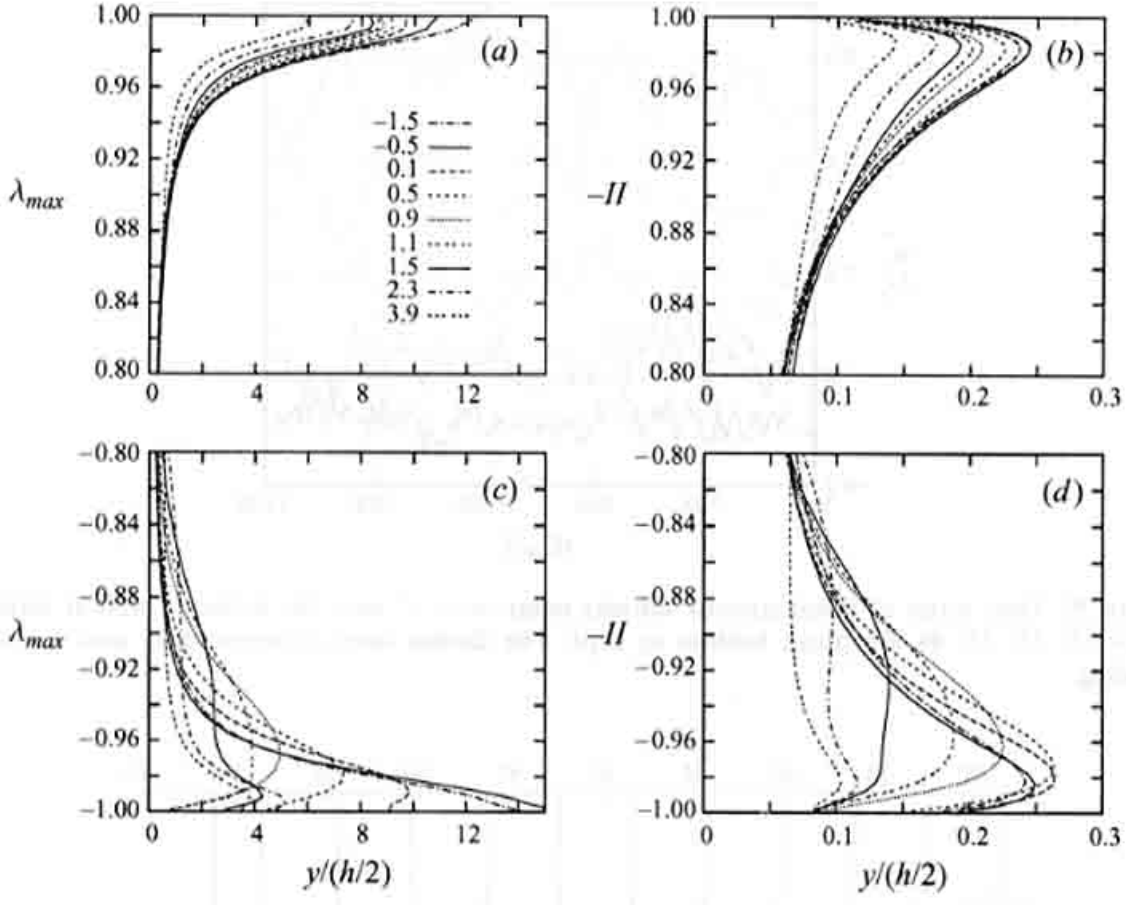

FIGURE 19. Maximum eigenvalue λ_{max} of the strain rate tensor (a,c), and second invariant $-II$ of the anisotropy tensor (b,d) versus wall distance normalized by half of the local duct height h such that walls are at $-1,1$ respectively. The line code for the streamwise location in units of x/δ is given in (a).

in predicting the correct relation of stress and strain tensors, e.g. the difference in the orientation of principal axes, could be tested in detail for a zone where both quantities change significantly.

5.2. *Unsteady separation process*

Unsteadiness induced by flow separation is of engineering interest, e.g. in the context of flow-induced vibrations. Limited information is currently available about the unsteady behaviour of separation bubbles. Na & Moin (1998) found that a separation bubble on a flat wall exhibits low-frequency unsteadiness. They did not find a regular shedding pattern at a distinct frequency as is the case for laminar bubbles (Pauley, Moin & Reynolds 1990). Rather, the unsteadiness of the bubble motion varied over a Strouhal number, $St_{\delta^*} = f\delta^*/U_0$, range 0.0025 to 0.01, where δ^* is the displacement thickness of the boundary layer upstream of separation.

Time series of the streamwise velocity at several locations near the deflected wall are shown in figure 20. It is difficult to identify a distinct frequency. In the rear part, an unsteady motion with a period of approximately $TU_b/\delta = 100$ emerges for a few cycles. The extent of the recorded time series is too short to decide whether this pattern reappears in a regular fashion. The corresponding Strouhal number based on the inlet channel centreline velocity and duct height 2δ is $St_H = 0.0175$. Using the maximum velocity and displacement thickness (computed at the deflected wall) ahead of separation at $x/\delta = 14$ we obtain $St_{\delta^*} = 0.014$, which is about 50% higher

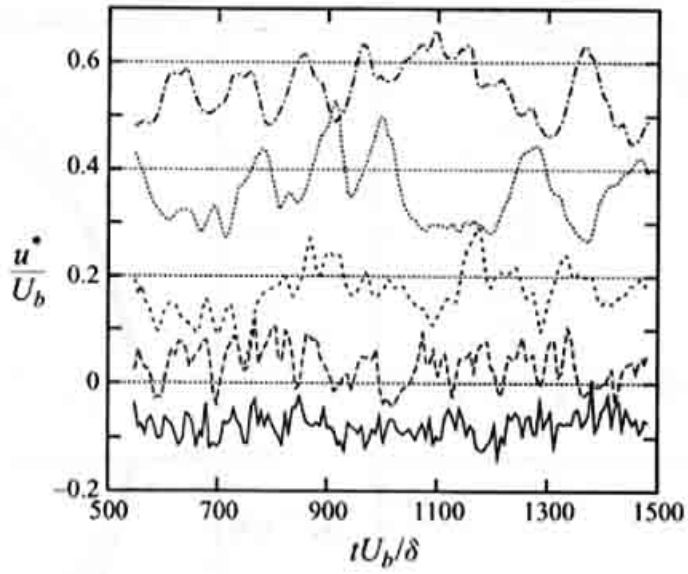

FIGURE 20. Time series of instantaneous velocity component u^* near the deflected wall at stations $x/\delta = 13, 22, 32, 48, 62$ (from bottom to top). The dotted lines correspond to zero for each recording.

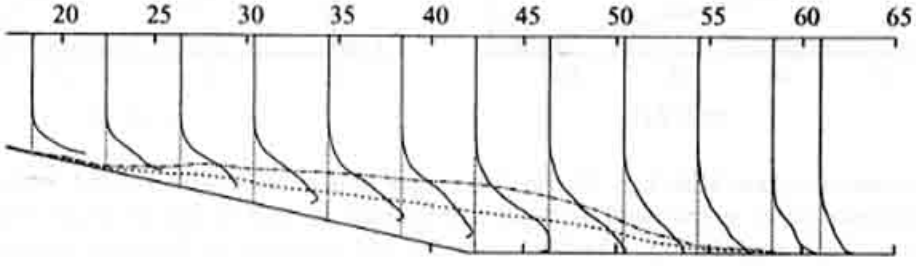

FIGURE 21. Reverse flow fraction (in percent) from case MED-W plotted as $x/\delta + 0.05 \times \gamma$, i.e. $\gamma = 100\%$ corresponds to 5 units on the horizontal axis. The dashed line marks the position where U crosses zero and the dividing streamline is marked with —·— .

than the maximum frequency found by Na & Moin (1998). The Strouhal number comparison is hindered by the fact that the time scale δ^*/U_{max} used to normalize the shedding frequency changes with x in the diffuser ahead of separation.

Frequency spectra recorded by Buice & Eaton (1996) in the outlet duct of the diffuser do not exhibit a peak at a distinct frequency. Masuda, Obi & Aoki (1994) made a similar observation. However, when they excited the flow through periodic blowing and suction through a slit at $x/\delta = 6.4$ they found that this excitation had the strongest effect on the downstream flow for a Strouhal number around $St_H = 0.026$. This is in the range where we observe 'natural' unsteadiness of the separation process in the diffuser rear part. Thus, our results corroborate the findings of Na & Moin (1998) that pressure-driven separation from a smooth wall is a highly unsteady process with a characteristic frequency range.

Figure 21 shows profiles of the reverse-flow fraction γ. The maximum height of the mean separation bubble is roughly one third of the duct cross-section. Instantaneous backflow occurs outside the dividing streamline which is derived from the temporally averaged flow field. This indicates that the flow in the rear part of the duct is influenced by large-scale motions which fill a considerable part of the cross-section. Probably, the vertical size of the bubble is also influenced by the presence of the opposite wall which interacts with these large scales. Maximum values of γ around

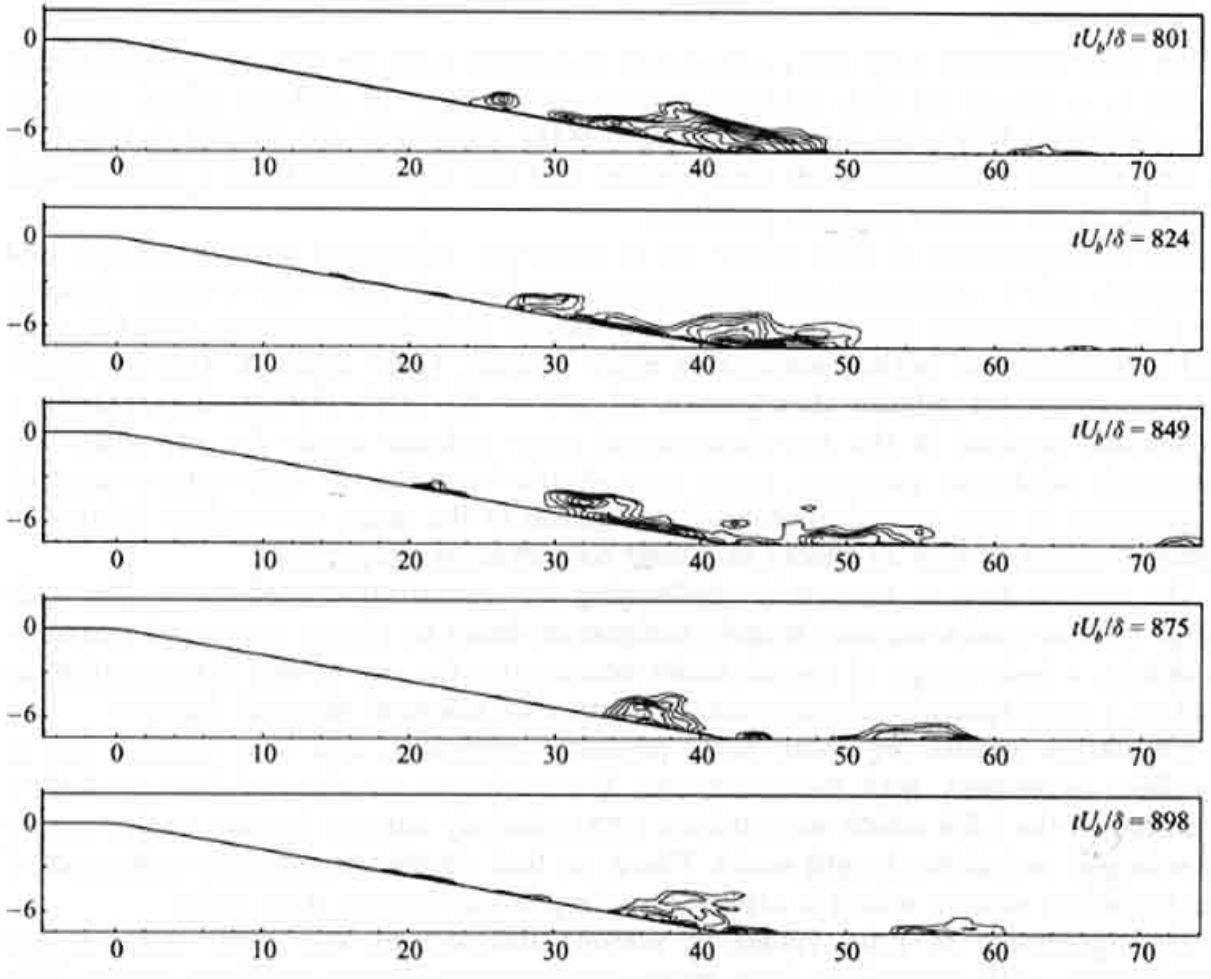

FIGURE 22. Series of contour plots showing regions of instantaneous flow reversal over a time period of about $100\delta/U_b$. The contour variable corresponds to negative values of the x-component of velocity averaged over the span.

82% are found a short distance from the wall in the corner region. Thus, there is no region in the diffuser where the flow is reversed all the time. The denomination 'separation bubble' therefore refers to one of several flow states which are found in the rear part, ranging from attached to temporarily separated flow.

Additional insight into the unsteady separation process is provided in figure 22 where a series of five plots show the evolution of the separation bubble over a time period of about $100\delta/U_b$. It is observed that the separation bubble originates near $x/\delta = 20$ as a small localized region of backflow. As this bubble is convected downstream it grows and reaches its maximum size at about $x/\delta = 50$ where the deflected diffuser wall meets the constant-area exit section. Beyond this point the bubble size diminishes and it virtually disappears by the time it reaches the exit boundary. Examination of instantaneous flow fields through visualization of pressure isosurfaces reveals that the growth of large-scale three-dimensional instabilities in the separated flow region plays a crucial role in the breakup of the bubble. Comparison of visualizations from wide and narrow domains shows that these large-scale instabilities develop quicker in the wide domain, thereby leading to a better predictions of mean velocity and stress profiles in the outlet duct.

6. Conclusions

We have used the large-eddy simulation technique with the dynamic subgrid-scale model to compute the flow through a plane, asymmetric 10°-diffuser which operates at a moderate Reynolds number of $Re_b = 9000$. An important feature of this flow is the gradual streamwise flow development and the separation from a smooth wall induced by an adverse pressure gradient.

The configuration is well suited for a thorough validation since geometry and upstream inflow conditions are unambiguously defined. Two experimental datasets for this configuration were examined. Both satisfy global conservation laws for mass and momentum to within reasonable error bounds. Only Buice & Eaton's (1997) measurements are reliable downstream of $x/\delta = 40$. Obi's (1993*a*) data exhibit a significant residual in the two-dimensional mass balance inside the tail duct. For thorough validation purposes, more care should be taken to demonstrate internal consistency of data, e.g. through local evaluation of the mean momentum balance at selected points as well as checks of global conservation properties.

The chosen flow is extremely challenging for quantitative prediction. The wide range of time scales requires lengthy integration times to obtain converged statistics. Similarly, a wide range of spatial scales necessitates the use of fine discretization as well as a large spanwise domain size to capture all essential physical features.

Simulation results for mean flow, pressure coefficient, and skin friction are in excellent agreement with measurements. Reattachment in the tail duct is slightly retarded in the LES which we attribute to a relatively narrow domain in this region of enlarged turbulence length scales. There, we find significant spanwise coherence of the turbulent motion which is expected to drop if the domain were wider.

The agreement of r.m.s.-values of velocity fluctuations and shear stress is less satisfactory, with deviations from measurements occasionally reaching up to 20% which is outside the measurement error bounds. The reasons for disagreement are not obvious since our results appear to be converged with respect to grid resolution. For a given mean flow the distribution of Reynolds stresses is not unique which highlights the need for careful and reliable measurements of Reynolds stresses.

The grid refinement study revealed the high sensitivity of this flow to the upstream conditions. Correct simulation of the flow entering the diffuser requires rather fine mesh spacings and small time steps. These requirements make an increase of domain width and overall simulation time – which would be desirable in order to capture all details of flow physics associated with the reattachment in the tail duct – prohibitively expensive.

Under the combined influence of geometry change, adverse and radial pressure gradients as well as a complicated strain history, the turbulence undergoes significant changes near the diffuser throat in the vicinity of the wall. Therefore, there is little hope that the mesh there can be significantly coarser than the mesh needed to produce correct turbulent inflow if results of similar quality are to be produced. The use of zonal meshes would help to reduce the cost of the simulation since spatial scales are much larger in the rear part than in the inlet duct.

At the resolution level employed, the SGS terms in the mean momentum balance are small, contributing a maximum of 8% to the total shear stress very close to the wall. However, the SGS model plays an essential role in the budget of turbulent kinetic energy, providing 40% of the total dissipation rate in the inlet duct and more than 80% in the tail duct, thereby adapting to the increase in turbulence level. The average model coefficient derived from the dynamic procedure corresponds to a Smagorinsky constant, $c_S = 0.12$.

Simulation results have provided insight into the physics of the separation process. Instantaneous backflow occurs on both walls immediately behind the throat. The large separation of the mean flow occurring about one third distance inside the expansion is preceded by a small stretch of detached flow immediately at the throat. There, a strong increase of pressure fluctuations and turbulence production is observed. We interpret the change in near-wall turbulence properties in this zone as being a result of the sudden change in geometry rather than being caused directly by the pressure gradient. Conversely, the separation in the rear part is a result of the accumulated flow deceleration through the presence of an adverse pressure gradient.

Separation in the rear part of the expansion is a low-frequency unsteady process involving large scales of motion which fill the entire cross-section. The separation bubble changes its size and position in a characteristic pattern. The unsteadiness is broadband and cannot be characterized through a single frequency. Immediately downstream of the separation bubble the flow is strongly disturbed with turbulent kinetic energy an order of magnitude higher than in equilibrium channel flow.

This work was supported in part by ONR grant N-00014-91-J-4072 (Program Officer: Dr L. Patrick Purtell). Computer time was provided by the NASA Ames Research Center, MSRC and ZIB. This work was supported in part by a grant of HPC time from the DoD at the Aeronautical Systems Center. We thank S. Obi, C. Buice and J. Eaton for making their experimental data available to us and for many stimulating discussions.

REFERENCES

AKSELVOLL, K. & MOIN, P. 1995 Large eddy simulation of turbulent confined coannular jets and turbulent flow over a backward facing step. *Rep.* TF-63. Dept. of Mech. Engng, Stanford University.

AKSELVOLL, K. & MOIN, P. 1996 Large eddy simulation of turbulent confined coannular jets. *J. Fluid Mech.* **315**, 387–411.

ALVING, A. E. & FERNHOLZ, H. H. 1996 Turbulence measurements around a mild separation bubble and downstream of reattachment. *J. Fluid Mech.* **322**, 297–328.

ASHJAEE, J. & JOHNSTON, J. P. 1980 Straight-walled, two-dimensional diffusers – transitory stall and peak pressure recovery. *Trans. ASME* I: *J. Fluids Engng* **102**, 275–282.

AZAD, R. S. 1996 Turbulent flow in a conical diffuser: a review. *Expl Thermal Fluid Sci.* **13**, 318–337.

BUICE, C. U. & EATON, J. K. 1996 Experimental investigation of flow through an asymmetric plane diffuser. *Annual Research Briefs – 1996*, pp. 243–248. Center for Turbulence Research, Stanford Univ./NASA Ames Research Center.

BUICE, C. U. & EATON, J. K. 1997 Experimental investigation of flow through an asymmetric plane diffuser. *TSD*-107. Dept. of Mech. Engng, Stanford University.

CABOT, W. 1994 Local dynamic subgrid-scale models in channel flow. *Annual Research Briefs – 1994*, pp. 143–159. Center for Turbulence Research, Stanford Univ./NASA Ames Research Center.

CHOI, H., MOIN, P. & KIM, J. 1992 Turbulent drag reduction: studies of feedback control and flow over riblets. *Rep.* TF-55. Thermosc. Div., Dept. of Mech. Engng, Stanford University.

DEAN, R. B. 1978 Reynolds number dependence of skin friction and other bulk flow variables in two-dimensional rectangular duct flow. *Trans. ASME* I: *J. Fluids Engng* **100**, 215.

DE ANGELIS, V., LOMBARDI, P. & BANERJEE, S. 1997 Direct numerical simulation of turbulent flow over a wavy wall. *Phys. Fluids* **9**, 2429–2442.

DENGEL, P. & FERNHOLZ, H. H. 1990 An experimental investigation of an incompressible turbulent boundary layer in the vicinity of separation. *J. Fluid Mech.* **212**, 615–636.

DURBIN, P. 1994 Separated flow computations with the k–ϵ–v^2 model. *AIAA J.* **33**, 659–664.

GERMANO, M., PIOMELLI U., MOIN P. & CABOT, W. H. 1991 A dynamic subgrid-scale eddy-viscosity model. *Phys. Fluids* A **3**, 1760–1765.

GHOSAL, S. 1996 An analysis of numerical errors in large-eddy simulation of turbulence. *J. Comput. Phys.* **125**, 187–206.

GHOSAL, S., LUND, T., MOIN, P. & AKSELVOLL, K. 1995 A dynamic localization model for large-eddy simulation of turbulent flows. *J. Fluid Mech.* **286**, 229–255.

GONG, W., TAYLOR, P. A. & DÖRNBRACK, A. 1996 Turbulent boundary-layer flow over fixed aerodynamically rough two-dimensional sinusoidal waves. *J. Fluid Mech.* **312**, 1–37.

JIMENEZ, J. & MOIN, P. 1991 The minimal flow unit in near-wall turbulence. *J. Fluid Mech.* **225**, 213–240.

KALTENBACH, H.-J. 1994 Large-eddy simulation of flow through a plane, asymmetric diffuser. *CTR Annual Research Briefs – 1994*, pp. 175–184. Center for Turbulence Research, Stanford Univ./NASA Ames Research Center.

KRAVCHENKO, A., MOIN, P. & MOSER, R. 1996 Zonal embedded grids for numerical simulations of wall-bounded turbulent flows. *J. Comput. Phys.* **127**, 412–423.

LESIEUR, M. & METAIS, O. 1996 New trends in large-eddy simulations of turbulence. *Ann. Rev. Fluid. Mech.* **28**, 45–82.

LILLY, D. K. 1992 A proposed modification of the Germano subgrid scale closure method. *Phys. Fluids* A **3**, 2746–2757.

LUND, T. S. & KALTENBACH, H.-J. 1995 Experiments with explicit filtering for LES using a finite-difference method. In *CTR Annual Research Briefs – 1995*, pp. 91–105. Center for Turbulence Research, Stanford Univ./NASA Ames Research Center.

LUND, T. S. & MOIN, P. 1996 Large eddy simulation of a concave wall boundary layer. *Intl J. Heat Fluid Flow* **17**, 290–295.

MAEDA, M., KASAGI, N., KUMADA, M., MIZOMOTO, M., NAGANO, Y. & TORII, K. 1995 Database on turbulent heat transfer. Dept. of Mech. Eng., Keio University, Yokohama, Japan (accessible via ftp-server ftp.mh.mech.keio.ac.jp).

MASS, C. & SCHUMANN, U. 1996 Direct numerical simulation of separated turbulent flow over a wavy boundary. In: *Notes on Numerical Fluid Mechanics*, vol. 52 (ed. E. H. Hirschel), pp. 227–241. Vieweg, Braunschweig.

MASUDA, S., OBI, S. & AOKI, K. 1994 Control of turbulent separating and reattaching flow by periodic perturbations. *Proc. ASME Fluids Engineering Division Summer Meeting on Turbulence Control, Lake Tahoe, USA*. FED-Vol. 193, pp. 55–61.

MITTAL, R. & BALACHANDAR 1997 On the inclusion of three-dimensional effects in simulations of two-dimensional bluff-body wake flows. *Proc. 1997 ASME Fluids Engineering Division Summer Meeting, Vancouver, Canada*. FEDSM97-3281.

MITTAL, R. & MOIN, P. 1997 Suitability of upwind-biased finite difference schemes for large-eddy simulation of turbulent flows. *AIAA J.* **35**, 1415–1417.

NA, Y. & MOIN, P. 1998 Direct numerical simulation of a separated turbulent boundary layer. *J. Fluid Mech.* **370**, 175–202.

OBI, S., AOKI, K. & MASUDA, S. 1993*b* Experimental and computational study of turbulent separating flow in an asymmetric plane diffuser. *Ninth Symp. on Turbulent Shear Flows, Kyoto, Japan, August 16–19, 1993*, p. 305.

OBI, S., OHIMUZI, H., AOKI, K. & MASUDA, S. 1993*a* Turbulent separation control in a plane asymmetric diffuser by periodic perturbation. In *Engineering Turbulence Modeling and Experiments 2* (W. Rodi & F. Martelli). Elsevier.

ORLANDI, P. 1989 A numerical method for direct simulation of turbulence in complex geometries. *CTR Annual Research Briefs – 1989*, pp. 215–229. Center for Turbulence Research, Stanford Univ./NASA Ames Research Center.

PAULEY, L. L., MOIN, P. & REYNOLDS, W. C. 1990 The structure of two-dimensional separation. *J. Fluid Mech.* **220**, 397–411.

PIOMELLI, U. 1993 High Reynolds number calculations using the dynamic subgrid-scale stress model. *Phys. Fluids* A **5**, 1484–1490.

ROGALLO, R. S. 1981 Numerical experiments in homogeneous turbulence. *NASA Tech. Mem.* 81315.

ROSENFELD, M., KWAK, D. & VINOKUR, M. 1991 A fractional step solution method for the unsteady incompressible Navier–Stokes equations in generalized coordinate systems. *J. Comput. Phys.* **94**, 102–137.

RUDERICH, R. & FERNHOLZ, H. H. 1986 An experimental investigation of a turbulent shear flow with separation, reverse flow, and reattachment. *J. Fluid Mech.* **163**, 283–322.

SCHMIDT, H. & SCHUMANN, U. 1989 Coherent structure of the convective boundary layer derived from large eddy simulation. *J. Fluid Mech.* **200**, 511–562.

SILVEIRA-NETO A., GRAND, D., METAIS, O. & LESIEUR, M. 1993 A numerical investigation of the coherent vortices in turbulence behind a backward-facing step. *J. Fluid Mech.* **256**, 1–25.

SIMPSON, R. L. 1989 Turbulent boundary-layer separation. *Ann. Rev. Fluid Mech.* **21**, 205–234.

SIMPSON, R. L., CHEW, Y.-T. & SHIVAPRASAD, B. G. 1981 The structure of a separating turbulent boundary layer. Part I. Mean flow and Reynolds stresses. *J. Fluid Mech.* **113**, 23–51.

SPALART, P. R., MOSER, R. D. & ROGERS, M. M. 1991 Spectral methods for the Navier–Stokes equations with one infinite and two periodic directions. *J. Comput. Phys.* **96**, 297–324.

STIEGLMEIER, M., TROPEA, C., WEISER, N. & NITSCHE, W. 1989 Experimental investigation of the flow through axisymmetric expansions. *Trans. ASME* I: *J. Fluids Engng* **111**, 464–471.

WANG, M., LELE, S. K. & MOIN, P. 1996 Computation of quadrupole noise using acoustic analogy. *AIAA J.* **34**, 2247–2254.

WEI, T. & WILLMARTH, W. W. 1989 Reynolds-number effects on the structure of a turbulent channel flow. *J. Fluid Mech.* **204**, 57–95.